Two-dimensional and three-dimensional computational models in hydrodynamic and morphodynamic...

Article *in* Hydrological Processes · March 2015

DOI: 10.1002/hyp.10277

CITATIONS
10

READS
244

7 authors, including:

Petteri Alho
University of Turku
80 PUBLICATIONS **1,046** CITATIONS
SEE PROFILE

Antero Kukko
Finnish Geospatial Research Institute
129 PUBLICATIONS **2,504** CITATIONS
SEE PROFILE

Hannu Hyyppä
Aalto University
164 PUBLICATIONS **3,423** CITATIONS
SEE PROFILE

Juha Hyyppä
422 PUBLICATIONS **9,660** CITATIONS
SEE PROFILE

HYDROLOGICAL PROCESSES
Hydrol. Process. (2014)
Published online in Wiley Online Library
(wileyonlinelibrary.com) DOI: 10.1002/hyp.10277

Two-dimensional and three-dimensional computational models in hydrodynamic and morphodynamic reconstructions of a river bend: sensitivity and functionality

Elina Kasvi,[1]* Petteri Alho,[1,2] Eliisa Lotsari,[3] Yunsheng Wang,[1] Antero Kukko,[4] Hannu Hyyppä[5,2] and Juha Hyyppä[4]

[1] *Department of Geography and Geology, University of Turku, FI-20014 Turku, Finland*
[2] *School of Engineering, Department of Real Estate, Planning and Geoinformatics, Aalto University, PO Box 15800, FI-00076 Aalto, Finland*
[3] *Department of Geographical and Historical Studies, University of Eastern Finland, PO Box 111, 80101 Joensuu, Finland*
[4] *Department of Remote Sensing and Photogrammetry, Finnish Geodetic Institute, PO Box 15, FI-02431 Masala, Finland*
[5] *Helsinki Metropolia University of Applied Sciences, PO Box 4011, FI-00079 Metropolia, Finland*

Abstract:

This study assesses hydrodynamic and morphodynamic model sensitivity and functionality in a curved channel. The sensitivity of a depth-averaged model to user-defined parameters (grain size, roughness, transverse bed slope effect, transport relations and secondary flow) is tested. According to the sensitivity analysis, grain size, transverse bed slope effect and sediment transport relations are critical to simulated meander bend morphodynamics. The parametrization of grain size has the most remarkable effect: field-based grain size parametrization is necessary in a successful morphodynamic reconstruction of a meander bend. The roughness parametrization method affects the distribution of flow velocities and therefore also morphodynamics. The combined effect of various parameters needs further research. Two-dimensional (2D) and three-dimensional (3D) reconstructions of a natural meander bend during a flood event are assessed against field measurements of acoustic Doppler current profiler and multi-temporal mobile laser scanning data. The depth-averaged velocities are simulated satisfactorily (differences from acoustic Doppler current profiler velocities 5–14%) in both 2D and 3D simulations, but the advantage of the 3D hydrodynamic model is unquestionable because of its ability to model vertical and near-bed flows. The measured and modelled near-bed flow, however, differed notably from each other's, the reason of which was left open for future research. It was challenging to model flow direction beyond the apex. The 3D flow features, which also affected the distribution of the bed shear stress, seem not to have much effect on the predicted morphodynamics: the 2D and 3D morphodynamic reconstructions over the point bar resembled each other closely. Although common features between the modelled and measured morphological changes were also found, some specific changes that occurred were not evident in the simulation results. Our results show that short-term, sub-bend scale morphodynamic processes of a natural meander bend are challenging to model, which implies that they are affected by factors that have been neglected in the simulations. The modelling of short-term morphodynamics in natural curved channel is a challenge that requires further study. Copyright © 2014 John Wiley & Sons, Ltd.

KEY WORDS morphodynamic modelling; sensitivity analysis; meandering; mobile laser scanning; ADCP; CFD

Received 9 January 2014; Accepted 18 June 2014

INTRODUCTION

Computational models capable of reproducing both hydrodynamic and morphodynamic features have become important tools for understanding the evolution of rivers. A simulation approach is attractive for solving environmental questions because of good spatial and temporal resolution and the ability to examine past (Alho *et al.*, 2010; Carling *et al.*, 2010) and hypothetical events (Verhaar *et al.*, 2008; Lotsari *et al.*, 2010). Despite their advantages, computational models are simplified representations of real-world phenomena, and there are often questions about the trade-off between sufficient field data, computational expensiveness and model reliability (Hardy *et al.*, 2003; Bates, 2004; Rodriguez *et al.*, 2004). The degree of the correspondence between a specific model run and its natural prototype depends on flow and sediment transport relationships, the topographic shape of the computational domain and the boundary conditions (BCs) for the open boundaries (Kleinhans, 2010; Schuurman *et al.*, 2013). Information about model functionality, sensitivity to user-based parametrization and sources of uncertainty is thus essential when solving environmental issues using computational modelling.

*Correspondence to: Elina Kasvi, Department of Geography and Geology, University of Turku, FI-20014 Turku, Finland.
E-mail: elina.kasvi@utu.fi

The most evident feature of a model is its dimensionality. Because one-dimensional model simulates flow only perpendicular to the river cross-section and averages the outputs cross-sectionally, the use of multidimensional models is recommended when modelling complex riverine environments (Carling *et al.*, 2010). Two-dimensional (2D) models have been shown to predict the general flow pattern in rivers relatively well (Alho and Mäkinen, 2010; Kasvi *et al.*, 2013a). They are also computationally lighter compared with three-dimensional (3D) models and require less extensive field investigations. Only 3D models, however, are capable of modelling vertical and, thus, spiral flow structures (Lane *et al.*, 1999; Lesser *et al.*, 2004). The effects of spiral flow can, however, be parameterized in a 2D approach to receive more reliable results (e.g. Nicholas, 2013; Schuurman *et al.*, 2013).

In addition to the dimension of the model, semi-empirical parametrization of physical processes may significantly affect the model outcome (Bates *et al.*, 1998; Lane *et al.*, 1999; Horrit *et al.*, 2006; Schuurman *et al.*, 2013). Many previous studies have found the application of spatially varying grain sizes to be important for the morphodynamic simulation results (Nicholas, 2000; Papanicolaou *et al.*, 2008; Nicholas, 2013; Lotsari *et al.*, 2014). The method and value of the roughness parametrization also have a significant effect on bed morphology (Nicholas, 2003; Lesser *et al.*, 2004; Schuurman *et al.*, 2013). For example, using a constant Chezy roughness value over a simulation domain, the roughness height becomes a function of the water depth causing variation in roughness across the area. Previous studies also suggest that using a spatially variable Manning coefficient could improve model performance (Nicholas, 2003). The effect of friction parametrization on the predicted morphodynamics, however, has not been explored largely (Schuurman *et al.*, 2013). Moreover, the formulation and parametrization of transverse bed slope effect, that is, the change in sediment transport in the downslope direction, such as that towards a pool, play an important role in morphodynamic modelling (Kleinhans, 2010; Nicholas, 2013; Schuurman *et al.*, 2013).

The accuracy of sediment transport formulae is generally considered poor (e.g. van Rijn, 1984a; Barry *et al.*, 2004; Schuurman *et al.*, 2013), however, Pinto *et al.* (2006) noted that the accuracy of simulated sediment transport is mainly determined by errors in current velocity and grain size distribution. The widely used van Rijn formula (1984a, b), in particular, was found to be very sensitive to physical properties such as flow velocity and grain size. Their study (Pinto *et al.*, 2006) suggests that hydrodynamic simulations used in sediment transport studies, especially in the case of the van Rijn formula, should be calibrated to errors in the velocity within 10%, to avoid large sediment transport errors, and that sediment transport is extremely sensitive to velocity close to the threshold of motion, that is, at low flow velocities. They also note that overestimates in velocity lead to larger errors in predicted sediment flux than underestimates in velocity. The transport formula by Engelund and Hansen (1967) was found to be less sensitive to the physical properties than the formula by van Rijn.

Various studies have applied computational models to curved channels. Alho and Mäkinen (2010) validated a 2D hydrodynamic model of a curved channel using field observations of bed formations. The model predicted the formations relatively well even on a reach with helical flow. However, Kasvi *et al.* (2013a) noted that a 2D model was not able to predict the fluvial characteristics that were responsible for the scroll bar formation at the inner bank, even though their model included a secondary flow correction. Lane *et al.* (1999) and Rodriguez *et al.* (2004) compared the hydrodynamic reconstructions of 2D and 3D models in a natural curved channel. Both studies showed that a 2D model reproduces the main flow characteristics but a 3D model is needed to model complex flow structures such as recirculation zones and the distribution of shear stresses. Other studies that have applied 3D hydraulic models to natural curved river reaches and assessed the results against field measurements have reported that the main flow patterns are predicted well qualitatively, but problems may occur in quantitative estimations of, for example, flow velocity (Hodkinson and Ferguson, 1998; Dargahi, 2004; Rodriguez *et al.*, 2004; Nicholas *et al.*, 2012).

Various model validation studies of meander evolution have been performed using flume tests as reference data (Shimizu *et al.*, 1990; Rüther and Olsen, 2007; Duan and Julien, 2010). These studies have claimed that morphodynamic models are capable of predicting the meander evolution and that both 2D (Duan and Julien, 2010) and 3D (Shimizu *et al.*, 1990; Rüther and Olsen, 2007) models may produce adequate results. Contrary to the findings of Kasvi *et al.* (2013a), Nicholas (2013) performed a depth-averaged morphodynamic simulation with secondary flow correction in which a straight channel developed a sinuous thalweg with point bars and scroll bars.

Models ultimately need to encompass real rivers, which are variable, dynamic and complex (Bates and Anderson, 2001; Rodriguez *et al.*, 2004; Hooke *et al.*, 2011). There have been some published studies applying 2D morphodynamic models to natural curved channels since the 1990s (e.g. Bridge, 1992; Darby *et al.*, 2002; Dargahi, 2004). Verhaar *et al.* (2008) stated that the best test for the accuracy of a morphodynamic model would be against a morphological survey of the river. In the studies presented earlier, however, model validation

DOI: 10.1002/hyp

has been based on cross-sectional topographical measurements, which have low accuracy and a high possibility of erroneous interpretation. A morphodynamic model validated with a digital terrain model (DTM), especially in a natural curved channel, is still a rarity, and to our knowledge, no study comparing the results of 2D and 3D morphodynamic models against high-resolution DTM of a natural meandering stream has been published.

In addition, the effects of either the parametrization of grain size, roughness and the transverse bed slope effect, or the selected sediment transport formula, on the morphodynamic reconstruction of a natural curved channel have barely been explored. It is also unclear how the 2D model, which neglects secondary circulation, differs from that which includes the correction for secondary circulation in its ability to model the meander bend morphodynamics. Finally, it is not yet known how satisfactorily the sub-bend morphological processes are reproduced in morphodynamic models and whether and how a 3D model provides an improved outcome compared with a 2D approach in a curved channel.

This study therefore aims to answer the following questions:

1. How does the parametrization of grain size, roughness and transverse bed slope influence the morphodynamic reconstruction of a natural river bend?
2. How sensitive is a morphodynamic model to the sediment transport formula or secondary flow correction in a curved channel?
3. How are the sub-bend scale hydrodynamic and morphodynamic processes reproduced over a natural meander point bar by 2D and 3D computational models?
4. What are the fluvio-morphological processes in a meander bend that are only evident in a 3D model?
5. Is it possible to exploit a morphodynamic model approach to reliably study curved channel evolution in a natural environment?

We apply 2D and 3D computational models to a natural meandering reach with a highly mobile sandy bed. First, we test the sensitivity of the 2D model over a river bend, to various user-defined parameters. Second, we model the hydrodynamics and morphodynamics of the same river bend over a bankfull flood event in 2D and 3D and compare the modelling results with detailed field measurements. The building, calibration and validation of the simulations are based on state-of-the-art field techniques including multi-temporal mobile laser scanning (MLS) and acoustic Doppler current profiler (ADCP).

FLUVIAL GEOMORPHOLOGY OF A MEANDER BEND

The curved shape of a meander bend causes peculiar 3D flow and sediment dynamics (Hooke, 1975). The concave bank of a meander bend is typically steep, whereas a gentle point bar forms on the convex side of the bend. In general, the high-velocity core (HVC) is situated near the convex bank at the entrance of the bend (e.g. Dietrich *et al.*, 1979). Thus, the stronger current flows over the point bar head, causing scour, chute bars and coarse grain sizes (e.g. McGowen and Garner, 1970; Bridge and Jarvis, 1976). The channel curvature and shoaling of the flow over the point bar force the HVC toward the concave bank (Leopold and Wolman, 1960) and cause an outward flow over the point bar head (Dietrich and Smith, 1983). The outward flow causes super-elevation of the water on the concave side, leading to secondary circulation: inward near-bed and outward near-surface velocity components, and downward flow close to the concave bank (e.g. Bridge and Jarvis, 1982; Termini and Piraino, 2011). The shift of the HVC and increase in depth over the point bar tail after crossing the bar crest decrease the bed shear stress on the downstream part of the point bar (McGowen and Garner, 1970; Dietrich and Smith, 1983). This, accompanied by a recirculation zone, which may occur at the point bar margin or along the inner bank beyond the bend apex (Frothingham and Rhoads, 2003; Kleinhans and van den Berg, 2011), causes filling and scroll bar formations over the point bar tail (Leopold and Wolman, 1960; Kasvi *et al.*, 2013b). Generally, coarser sediment can be found around the thalweg, point bar head and chute, whereas fine material is deposited over the point bar tail and top. These processes make meander evolution a complicated phenomenon in nature, with various open research questions. Numerical modelling is thus an attractive but also challenging tool with which to investigate meander dynamics.

MATERIAL AND METHODS

Hydrodynamic equations

Our hydrodynamic modelling is based on Navier–Stokes' shallow water equations for an incompressible fluid in two and three dimensions (Delft3D-FLOW). The model is fully non-linear and physics-based. Modelling is implemented on a curvilinear, unstructured grid. We use both 2D and 3D simulations. In 3D simulation, the vertical grid consists of layers separated by σ-planes, which follow the bottom topography and the free surface. The number of layers is constant over the computational area, which makes the layer thickness non-uniform. For each σ-layer, a set of conservation equations is solved. The vertical momentum equation is reduced to the

DOI: 10.1002/hyp

hydrostatic pressure equation (shallow water assumption) as the vertical accelerations are assumed to be small compared with gravitational acceleration. It reads as follows:

$$\frac{\partial P_{\mathrm{h}}}{\partial \sigma} = -\rho g h \tag{1}$$

where P_{h} is the hydrostatic pressure and σ is the vertical sigma coordinate.

In 3D simulation, the horizontal momentum equations in the x (Equation (2)) and y (Equation (3)) directions are as follows:

$$\frac{\partial u}{\partial t} + u\frac{\partial u}{\partial x} + v\frac{\partial u}{\partial y} + \frac{\omega}{d}\frac{\partial u}{\partial \sigma} - cv = -\frac{1}{\rho_0}P_x + \frac{1}{d^2}\frac{\partial}{\partial \sigma}\left(V_{\mathrm{v}}\frac{\partial u}{\partial \sigma}\right) + V_{\mathrm{h}}\left(\frac{\partial^2 u}{\partial x^2} + \frac{\partial^2 u}{\partial y^2}\right) \tag{2}$$

$$\frac{\partial v}{\partial t} + u\frac{\partial v}{\partial x} + v\frac{\partial v}{\partial y} + \frac{\omega}{d}\frac{\partial v}{\partial \sigma} - cu = -\frac{1}{\rho_0}P_y + F_y + \frac{1}{d^2}\frac{\partial}{\partial \sigma}\left(V_{\mathrm{v}}\frac{\partial v}{\partial \sigma}\right) + V_{\mathrm{h}}\left(\frac{\partial^2 v}{\partial x^2} + \frac{\partial^2 v}{\partial y^2}\right) \tag{3}$$

If flow is solved in three dimensions, spiral flow also emerges in the model outcome. As the spiral flow motions are important in curved channels, the effect of secondary flow is included in the 2D simulation. The depth-averaged momentum equations in the 2D simulation read:

$$\frac{\partial u}{\partial t} + u\frac{\partial u}{\partial x} + v\frac{\partial u}{\partial y} + g\frac{\partial h}{\partial x} - cv + F_{\mathrm{sec},x} = -\frac{1}{\rho 0}P_x + V_{\mathrm{h}}\left(\frac{\partial^2 u}{\partial x^2} + \frac{\partial^2 u}{\partial y^2}\right) \tag{4}$$

$$\frac{\partial v}{\partial t} + u\frac{\partial v}{\partial x} + v\frac{\partial v}{\partial y} + g\frac{\partial h}{\partial y} - cv + F_{\mathrm{sec},y} = -\frac{1}{\rho 0}P_y + V_{\mathrm{h}}\left(\frac{\partial^2 v}{\partial x^2} + \frac{\partial^2 v}{\partial y^2}\right) \tag{5}$$

where u and v are the velocity components in the Cartesian coordinate system ($\mathrm{m\,s^{-1}}$), g is the gravitational acceleration ($\mathrm{m\,s^{-2}}$), c is the Coriolis coefficient ($\mathrm{s^{-1}}$), $P_{x,y}$ is the pressure, F_{sec} is the effect of secondary flow on depth-averaged velocity, d is the water depth (m), ρ_0 is the reference density of water ($\mathrm{kg\,m^{-3}}$), ω is the vertical velocity component in the σ-coordinate system ($\mathrm{m\,s^{-1}}$), V_{v} is the vertical eddy viscosity (computed by k–e), and V_{h} is the horizontal eddy viscosity (user defined).

The final terms of Equations (2)–(5) represent the horizontal Reynolds stresses. Assuming a constant density of water, the pressure gradients are calculated as follows:

$$P_x = g\frac{\partial h}{\partial x} + \frac{\partial p}{\rho_0 \partial x} \tag{6}$$

$$P_y = g\frac{\partial h}{\partial y} + \frac{\partial p}{\rho_0 \partial y} \tag{7}$$

where p is the atmospheric pressure and h is the water level.

The effect of secondary flow on the depth-averaged velocity is calculated as follows:

$$F_{\mathrm{sec},x} = \frac{gu\sqrt{u^2+v^2}}{{C_{2D}}^2 h} \tag{8}$$

$$F_{\mathrm{sec},y} = \frac{gv\sqrt{u^2+v^2}}{{C_{2D}}^2 h} \tag{9}$$

where C is Chezy's coefficient.

The horizontal continuity equation (conservation of mass) is given by

$$\frac{\partial \zeta}{\partial t} + \frac{\partial [h\overline{u}]}{\partial x} + \frac{\partial [h\overline{v}]}{\partial y} = 0 \tag{10}$$

where ζ is the water surface elevation (m) and $\overline{u}$ and $\overline{v}$ are the depth-averaged velocity components ($\mathrm{m\,s^{-1}}$).

Assuming hydrostatic pressure distribution, the vertical velocity is computed from the continuity equation as follows:

$$\frac{\partial W}{\partial \sigma} = -\frac{\partial \zeta}{\partial t} - \frac{\partial [hu]}{\partial x} - \frac{\partial [hv]}{\partial y} \tag{11}$$

where W is the vertical velocity relative to the σ-plane (in $\mathrm{m\,s^{-1}}$).

In Delft3D, three approaches to bed roughness parametrization are given: Chezy's, Manning's and White–Colebrook's approaches. In this study, we test each of the approaches. When the Chezy roughness formulation is used, the roughness height becomes a function of the water depth, leading to variation in roughness. For example, a uniform Chezy roughness means greater Nikuradse k_{s} roughness length in deeper channels. Thus, the roughness parametrizations have different effects on the simulation outcome, and they can all be linked to each other.

Chezy and Manning's n are related to each other as follows:

$$C = \frac{\sqrt[6]{H}}{n} \tag{12}$$

Chezy and Nikuradse k_{s} relate as follows:

$$C = 18\log\left(\frac{12H}{k_{\mathrm{s}}}\right) \tag{13}$$

DOI: 10.1002/hyp

where C is Chezy's roughness coefficient for 2D model ($\mathrm{m\,s^{-2}}$), H is the water depth (m), n is Manning's roughness coefficient, and k_s is Nikuradse's roughness length (White–Colebrook's approach) (m).

There is also a difference between the 2D and the 3D Chezy coefficients, which depends on the relative thickness of the computational bottom layer in the 3D model. It is possible to use a 2D simulation for the calibration of water levels for a 3D approach if the velocity profile is almost logarithmic, a condition that can be assumed in this study.

We used an alternating direction implicit (ADI) method (a finite difference method) to solve the momentum and continuity equations (Leendertse and Liu, 1975). The ADI-method splits a single time step into two stages, both of which consist of half a time step. In the first stage, the v-momentum equation (Equation (2) or (4)) is solved, followed by the u-momentum equation (Equation (3) or (5)), which is implicitly coupled with the continuity equation (Equation (10)) by the free surface gradient. In the second stage, first, the u-momentum equation is solved, followed by the v-momentum equation, which is implicitly coupled with the continuity equation by the free surface gradient. For the 3D shallow water equations, the horizontal velocity components are coupled in the vertical direction by the vertical advection and viscosity term. In the 2D approach, the vertical flow is parameterized to include the effect of spiral flow induced by streamline curvature.

For the spatial discretization of the horizontal advection terms, we used a so-called cyclic method (Stelling and Leendertse, 1992), in which the horizontal advection terms are approximated by the sum of a third-order upwind scheme and a second-order central scheme. A second-order central scheme is applied for approximation of the vertical advection term. Time integration is based on the ADI method.

Morphodynamic equations

In this study, we use two different approaches to model the sediment transport, those of van Rijn (1993) (hereby VR) and Engelund and Hansen (1967) (hereby EH). We selected the VR approach to model the sediment transport because it is suitable for the sediment size at the study site (D_{50} 0.05–2 mm) and it has separate expressions for bed-load and suspended load. The sediment modelling approaches by van Rijn are also the most physics-based of the widely used transport relations and thus often regarded as the best (Pinto *et al.*, 2006). The EH approach was, by contrast, selected because it is one of the simplest transport formulas and thus is not as sensitive to errors in the physically based parameters of the model (Pinto *et al.*, 2006). The sediment calculations in Delft3D are based on hydrodynamic calculations from the previous half time step.

Van Rijn approach. The suspended sediment transport is calculated by solving the 3D advection–diffusion equation for the suspended sediment (the fourth and seventh terms describe the vertical gradients and thus the terms disappear in the depth-averaged approach):

$$\frac{\partial c}{\partial t}+\frac{\partial uc}{\partial x}+\frac{\partial vc}{\partial y}+\frac{\partial (W-W_s)}{\partial x} = \frac{\partial}{\partial x}\left(D_x\frac{\partial c}{\partial x}\right)+\frac{\partial}{\partial y}\left(D_y\frac{\partial c}{\partial y}\right)+\frac{\partial}{\partial z}\left(D_z\frac{\partial c}{\partial z}\right)+S \quad (14)$$

where W_s is the sediment settling velocity ($\mathrm{m\,s^{-1}}$), c is the sediment concentration ($\mathrm{kgm^{-3}}$), D is the eddy diffusivity, and S is the source/sink term describing the erosion and deposition fluxes (Equation (21)).

In Delft3D, the sub-grid scale mixing coefficients (horizontal and vertical viscosity, i.e. V_h and V_v, and diffusivity, i.e. D_h and D_v) are assumed to consist of three parts: 2D turbulence, 3D turbulence and kinematic viscosity (Delft3D-FLOW, 2011, p. 199); 2D turbulence determines the horizontal mixing and 3D turbulence the vertical mixing. In 2D simulation, to maintain model stability, constant eddy viscosity and diffusivity coefficients were used, which determine the combined effect of 2D and 3D turbulences and the kinematic viscosity. In a 3D simulation, the kinematic viscosity was set to 1.4 E-06 $\mathrm{m^2\,s^{-1}}$ and constant values were used to determine the 2D turbulence V_h and D_h; 3D tubulence was based on the k– ϵ turbulence closure model (Delft3D-FLOW, 2011, p. 231). In that case, the vertical sediment mixing coefficient (eddy diffusivity) was calculated from the vertical eddy viscosity by the k–ϵ model:

$$D_v = \beta V_v \quad (15)$$

where β is van Rijn's beta factor of sediment fraction and V_v is the vertical eddy viscosity.

The van Rijn's beta factor is calculated as follows:

$$\beta = 1 + 2\left(\frac{w_s}{u_{*,c}}\right)^2 \quad (16)$$

where w_s is the the sediment fall velocity ($\mathrm{m\,s^{-1}}$) and $u_{*,c}$ is the current-related bed shear velocity ($\mathrm{m\,s^{-1}}$).

The fall velocity of the suspended sediment depends on the sediment diameter and is computed as follows:

$$w_s = \begin{cases} \dfrac{(s-1)gD_s^2}{18V_k} & 65\ \mu\mathrm{m} < D_s \le 100\ \mu\mathrm{m} \\ \dfrac{10V_k}{D_s}\left(\sqrt{1+\dfrac{0.01(s-1)gD_s^3}{{V_k}^2}}\right) & 100\ \mu\mathrm{m} < D_s \le 1000\ \mu\mathrm{m} \\ 1.1\sqrt{(s-1)gD_s} & 1000\ \mu\mathrm{m} < D_s \end{cases} \quad (17)$$

DOI: 10.1002/hyp

where s is the relative density of sediment ($\mathrm{kgm^{-3}}$), D_s is the diameter of sediment in suspension (m), and V_k is the kinematic viscosity coefficient of water ($\mathrm{m^2\,s^{-1}}$).

The transfer of sediment between the bed and the flow is modelled using sink and source terms acting near the bed, above the so-called van Rijn reference height (van Rijn, 1993). Bed-load transport occurs below the reference height and suspended-load transport above it. The sediment concentrations below the reference layer are assumed to adjust to the same concentration as the reference layer. The sediment concentration in the reference layer is calculated as follows:

$$c_a = f_{sus} 0.015 \rho_s \frac{D_{50} {T_a}^{1.5}}{a {D_*}^{0.3}} \tag{18}$$

where f_{sus} is the calibration parameter (2.0 in this study), c_a is the sediment concentration at reference height ($\mathrm{kg\,m^{-3}}$), ρ_s is the density of sediment particles ($\mathrm{kg\,m^{-3}}$), D_{50} is the median sediment diameter (m), and T_a is the dimensionless bed shear stress.

The quantity of sediment entering the flow due to upward diffusion (source) from the reference layer and the quantity of sediment dropping out of the flow (sink) due to sediment settling are modelled at each half time step. We assumed a linear concentration gradient between the reference height and the reference layer. The required source and sink terms for the reference layer are calculated as follows:

$$Source = \frac{D_v c_a}{\Delta z} \tag{19}$$

$$Sink = c_{rl}\left(\frac{D_v}{\Delta z} + w_s\right) \tag{20}$$

where D_v is the vertical eddy diffusivity, c_{rl} is the mass concentration of sediment in the reference layer ($\mathrm{kg\,m^{-3}}$), and Δz is the vertical distance of the reference layer from the reference height a (m).

Because of the suspended sediment transport, the bottom sediment change at location (x,y) ($\mathrm{kg\,m^{-2}}$) is

$$\Delta S_{bed,s}^{(x,y)} = (Sink - Source)\Delta t \tag{21}$$

The magnitude (Equation (22), $\mathrm{kg\,m^{-1}\,s^{-1}}$) and direction (Equations (23) and (24)) of bed-load transport are computed as follows:

$$|S_b| = f_{bed} 0.5 n \rho_s d_{50} u_*^{'} D_*^{-0.3} T \tag{22}$$

$$S_{b,x}^{''} = \frac{u_b}{|q_b|}\left|s_b^{''}\right| \tag{23}$$

$$S_{b,y}^{''} = \frac{v_b}{|q_b|}\left|s_b^{''}\right| \tag{24}$$

where f_{bed} is the calibration parameter (1.2 in this study), n is the availability of sediment, u' is the effective bed shear velocity (based on the velocity in the bottom layer), D_* is the dimensionless particle diameter, T is the dimensionless bed shear stress (based on the velocity in the bottom layer), u_b and v_b are the (near-bed) flow velocity components (depth-averaged in 2D approach), and q is the (near-bed) flow velocity (depth-averaged in 2D approach).

The bed-load transport vectors are then relocated from water level points to velocity points using an 'upwind' computational scheme, which ensures numerical stability (Lesser *et al.*, 2004).

Engelund and Hansen approach. When using the EH approach, the advection–diffusion formula is not used for sediment transport because the EH only models the bed-load transport. According to Engelund and Hansen (1967), the bed-load transport rate is

$$S_b = \frac{0.05 q^5}{\sqrt{g} C^3 \Delta^2 D_{50}} \tag{25}$$

where Δ is the relative density of sediment under water.

In the case of a depth-averaged simulation, the secondary flow intensity is computed by the flow module, and it affects the direction of the bed-load transport. The direction of the sediment transport (taking secondary flow effect into account) is calculated from the following equation:

$$\tan(\gamma_\tau) = \frac{v - \alpha_I \overset{u}{U} I_S}{u - \alpha_I \overset{v}{U} I_S} \tag{26}$$

in which

$$\alpha_I = \frac{2}{\kappa^2}\left(1 - \frac{1}{2}\frac{\sqrt{g}}{\kappa C}\right) \tag{27}$$

where I_s = spiral flow intensity ($\mathrm{m\,s^{-2}}$), γ is the angle between downstream and sediment transport direction, κ is the Von Kàrmàn constant, and U is the depth-averaged velocity.

Transverse bed slope effect. Bed-load transport is affected by bed level gradients. Two bed slope directions are distinguished: the slope in the initial direction of the transport (referred to as the longitudinal bed slope) and the slope in the direction perpendicular to that (referred to as the transverse bed slope). The transverse component of the bed-load transport is calculated as follows:

DOI: 10.1002/hyp

$$S_{b,x} = \left|S_b^{'}\right| \alpha_{bn} \frac{u_{cr}}{|\overrightarrow{u_b}|} \frac{\partial z_b}{\partial n} \tag{28}$$

where $\left|S_b^{'}\right|$ is the magnitude of the unadjusted bed-load transport, α_{bn} is the user-defined coefficient (default is 1.5, values 0, 1.5 and 3 are tested in this study), u_{cr} is the critical (near-bed) velocity, $|\overrightarrow{u_b}|$ is the (near-bed) fluid velocity vector, and $\frac{\partial z_b}{\partial n}$ is the bed slope (normal to the unadjusted bed slope transport vector).

Change in the bed sediment due to bed load. The change in the bottom sediment caused by the bed-load transport is calculated as follows:

$$\Delta S_{bed,b}^{(x,y)} = \left(S_{b,x}^{(x,y-1)} \Delta y^{(x,y-1)} - S_{b,x}^{(x,y)} \Delta y^{(x,y)} + S_{b,y}^{(x-1,y)} \Delta x^{(x-1y)} - S_{b,y}^{(x,y)} \Delta x^{(x,y)}\right) \frac{\Delta t}{A^{(x,y)}} \tag{29}$$

where $S_{bed,b}^{(n,m)}$ is the bottom sediment change due to bed-load (kg m^{-2}), Δt is the time step (s), $A^{(n,m)}$ is the area of computational cell (m^2), $S_{b,x,y}^{(n,m)}$ is the bed-load transport vector in the x and y directions (kg m^{-1} s^{-1}), and $\Delta y^{(n,m)}$ is the cell width in the y direction (m).

The change occurring in the mass of bed material as a result of the suspended-load and bed-load transports is calculated at each time step as the sum of Equations (21) and (29) in the VR approach and simply by Equation (29) in the EH approach. This change in mass is translated into a bed-level change, and the updated bed level is again used for the following hydrodynamic calculation.

Field survey

The study was carried out in Northern Finland on the river Pulmanki (Figure 1a). The river is meandering and unregulated and has a mobile, sandy bed (D_{50} 0.05–2 mm). We simulated the hydrodynamic and morphodynamics of the spring flood in 2010 along a reach of 2100 m and focused on one meander bend (Figure 1b). During the modelling period of 22 May to 7 June, the discharge decreased gradually from 45 m^3 s^{-1} to 9 m^3 s^{-1}. The point bar was completely inundated during the flood, and was exposed by 7 June. With a bankfull discharge of 45 m^3 s^{-1}, the peak water level was ~2 m higher than at the end of the modelling period.

To build, calibrate and validate the models, an extensive field measurement campaign was undertaken. We surveyed the initial geometry using an interferometric scanning sonar and MLS. The main channel, which is also inundated during the low water stage, was surveyed immediately after the ice break in May 2010 using the

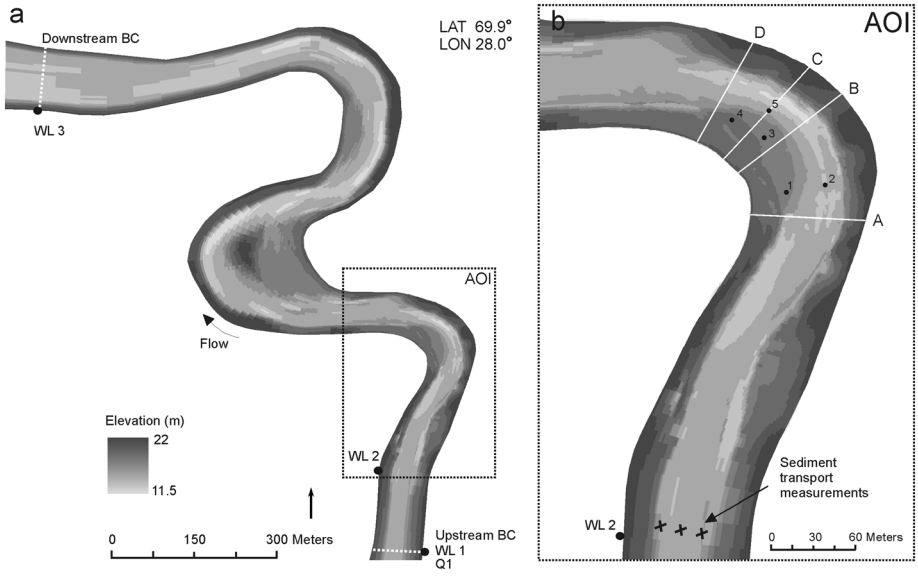

Figure 1. Study area: (a) The entire modelled reach (sinuosity ~1.4). The water level (WL 1–3) and discharge (Q1) measurement stations, as well as upstream and downstream boundaries, are marked in the figure. The grid and topography are used in the simulation. Note that the upstream boundary is 300 m away from the area of interest; (b) the area of interest. The locations of sediment transport measurements are marked with crosses. The white lines represent the four river cross-sections for which hydraulic characteristics are dissected in Results. Points 1–5 are observation points that are used to dissect the differences between the modelling results in the sensitivity analysis

DOI: 10.1002/hyp

sonar (Aquatic Sonar's Swathe Surveyor), which consists of two side-looking and one downward-looking transducers. The data was collected with a point spacing of 0.25 m. The point bars and banks were surveyed using MLS before the winter on 2009, and the geometry was assumed to remain unchanged, being frozen under the snow during the winter. The data was collected using a FARO Photon 80 mounted on a cart to speed up the data collection process. The MLS system was composed of a temporally synchronized LiDAR sensor, GPS receivers and an inertial measurement unit. A scanning frequency of 30 Hz and point frequency of 120 Hz were used. An average point density of 7400 points/m^2 and standard deviation of error of 0.04 m were achieved. A full accuracy assessment of the pre-flood MLS data is presented in Kasvi *et al.* (2013b).

A curvilinear, unstructured grid representing the initial geometry was built for the hydrodynamic and morphodynamic models based on the sonar and MLS data (Figure 1a). Orthogonal co-ordinates were used. Because the grid resolution has a major effect on the model predictions (e.g. Bates *et al.*, 1998), a higher mesh resolution was used in the area of interest (AOI): the cell size was between 0.7 and 0.9 m^2 on the point bar and between 0.9 and 1.7 m^2 in the main channel. In the area outside the AOI, the cell size was varied between 3 and 10 m^2. In the areas where the data density was greater than the cell size, the grid cell elevation value was averaged on the basis of the values falling inside a grid cell. We used triangular interpolation in the other areas.

To evaluate the functionality of the morphodynamic models, we also surveyed the post-flood geometry of the point bar in the AOI. We used a ROAMER MLS system, mounted on a cart, with 49-Hz scanning and 244-kHz point measurement frequencies, resulting in an average point density of 6500 points/m^2 and a standard deviation of error of 0.0145 m. The full data processing and accuracy assessment of the post-flood MLS data are presented in Flener *et al.* (2013). On the basis of the pre-flood and post-flood MLS point clouds, we created 0.2 m × 0.2 m DTMs representing the point bar using GIS software. By subtracting the DTMs from each other, we created a DTM of difference, representing the flood-based changes that occurred on the point bar (Figure 6).

As the water surface elevations were used as the downstream BC in the hydrodynamic model, the water-level changes were recorded at 15-min intervals (WL 3 in Figure 1a) during the flood on May 2010. We used a Solinst Levelogger Gold (Model 3001), which has an accuracy of 0.05%. The variation in water level was tied to a geographic coordinate system using RTK–GPS. A water-level record, located inside the AOI (WL 2 in Figure 1a), was used to calibrate the hydrodynamic model. For the upstream BC (location shown in Figure 1a), we built a discharge rating curve. We measured the discharge at the upstream boundary four times during the flood event (duration of 13 days), using an ADCP (Son-Tek RiverSurveyor M9). We then based the discharge rating curve on the relationship between the discharge and the water level record (WL 1) at the upstream boundary. For analysis of the results of the 2D and 3D hydrodynamic models, we measured 3D flow fields along three cross-sections (i.e. A, C and D) in the AOI, using an ADCP attached to a rubber boat. The boat speed was kept lower than the flow velocities during the measurement. The ADCP M9 has a velocity profiling range of up to 30 m and a discharge measurement range of 80 m. The sensor consists of four 3-MHz and four 1-MHz velocity measurement transducers. The final measurement value is averaged from all eight beam pulses, which have a recording frequency of 1 Hz. The cell size of a measurement is defined automatically by the device depending on the boat and flow velocity. In this study, the cell side lengths varied between 0.1 and 0.2 m. The flow field is not measured at distances less than ~0.25 m from either the riverbed (side lobe interference) or the water surface (blanking distance) (Szupiany *et al.*, 2007). The depth is measured by an integrated 0.5-MHz echo sounder. The location of the ADCP was measured with an integrated GPS (Global Positioning System) device, which minimises location and flow velocity measurement errors caused by moving bed (Muste *et al.*, 2004). The noise of the ADCP data was reduced by increasing the data network density of each section to contain 1000 data points in both the vertical and horizontal directions. Next, values for streamwise velocity components were resampled for each data point by averaging clusters of 100 × 100 points. New values for the cross-stream velocity components were counted by averaging clusters of 5 × 5 data points. The flow data were then plotted on cross-sectional figures, where isolines and vectors represented the streamwise and cross-stream flow, respectively.

The initial grain size distribution was based on 210 sediment samples. We realized significantly denser sampling over the AOI (sample spacing ~2 m) compared with the area outside the AOI (sample spacing ~30–40 m). The locations of the samples were measured using an RTK–GPS, and the D_{50} values were interpolated to cover the whole area. We also measured the bed-load and suspended load transport rates for the morphodynamic model calibration. The bed-load transport rate was measured using a Helley-Smith sampler at three verticals along a cross-section upstream of the AOI during two flow stages. We took three samples of 6-min duration from each of three verticals and took their average value. On the basis of these measurements, the total bed-load

DOI: 10.1002/hyp

transport ($m^3 s^{-1}$) across the section was calculated. On the basis of previous studies, we assumed a hydraulic efficiency of 1.5 (Hubbell, 1987; Blizard and Wohl, 1998). At the same time, suspended load was measured using a depth-integrated water sampler. One sample was taken at each location and discharge (locations shown in Figure 1).

Sensitivity analysis and execution of the computational models

To test the sensitivity of the hydrodynamic and morphodynamic models to several user-dependent parameters, a sensitivity analysis was carried out with the 2D model (Table I). Some of the parameters were first calibrated to find the best values for the sensitivity analysis. Manning's n, Nikuradse k_s, Chezy's roughness and sediment transport factors as well as the horizontal eddy diffusivity and viscosity were adjusted. The models were tested against the water level (WL2) and ADCP-based flow velocity measurements and measured sediment transport rates (Table II). The most suitable roughness values were 0.03, 55 and 0.04 for Manning, Chezy and Nikuradse, respectively. Constant values of horizontal eddy diffusivity and viscosity were used to maintain model stability; they were set to 0.04 and $0.07\,m^2 s^{-1}$, respectively. For optimizing the agreement between measured and modelled (van Rijn) transport rates, we adjusted the transport magnitude factors to 1.2 and 2.0 in the calibration process for bed-load and suspended load respectively (term f_{bed} in Equation (22) and term f_{sus} in Equation (18)) according to the comparisons between the measured and modelled transport magnitudes (Table II).

Table II. During the calibration process, morphodynamic models were assessed against field-based bed-load transport rates ($m^3 s^{-1}$) of two different discharges: high ($45\,m^3 s^{-1}$) and moderate ($28\,m^3 s^{-1}$). The field measurements were corrected assuming a factor of 1.5 in the measured bed-load transport (cf. Hubbell, 1987; Blizard and Wohl, 1998). This table shows the measured and modelled bed-load transport rates during two discharges

Discharge	Field-based bed-load transport	Corrected field-based bed-load transport	Modelled bed-load transport
$45\,m^3 s^{-1}$	1.12×10^{-4}	7.4×10^{-5}	8.8×10^{-5}
$28\,m^3 s^{-1}$	7.6×10^{-5}	5.07×10^{-5}	1.5×10^{-6}

In the sensitivity analysis, the relative effects of the parametrizations to the modelling results were assessed. First, we ran the model with default parameters (Run 1), that is, a uniform sediment diameter, a constant Manning's roughness, medium transverse bed slope effect, van Rijn's (1993) sediment transport formulation and secondary flow correction. In other runs, only one parameter deviated from the default run. In the second run, we tested the morphodynamic model sensitivity to the definition of grain size distribution by running the model with a spatially varying (field measurement-based) grain size distribution (Run 2). Third, we tested the sensitivity of the hydrodynamic and morphodynamic models to three different roughness parametrization approaches (Runs 3a–c). We also tested a spatially varying Manning's roughness parameter approach, in which the roughness values were based on the bed material and bed characteristics so that the values were

Table I. Model runs of the sensitivity analysis. The parameters of Run 1 are the default parameters, which are used in all other runs: only the parameter under examination deviates from the default run

	Run 1	Run 2	Run 3a	Run 3b	Run 3c	Run 4a	Run 4b	Run 5	Run 6
Grain size									
Constant (0.03 mm)	x		x	x	x	x	x	x	x
Varying		x							
Roughness									
Constant manning (0.03)	x	x				x	x	x	x
Constant Chezy (55)			x						
Constant k_s (0.04)				x					
Varying Manning					x				
Transverse bed slope effect									
High (factor = 3)						x			
Medium (factor = 1.5)	x	x	x	x	x			x	x
Low (factor = 0)							x		
Transport formula									
VR	x	x	x	x		x	x		x
EH								x	
Secondary flow									
Yes	x	x	x	x		x	x	x	
No									x

DOI: 10.1002/hyp

between 0.01 and 0.02 on the point bar and channel, and between 0.03 and 0.04 near the banks. Fourth, we tested the effect of transverse bed slope parametrization to the morphodynamic model (Runs 4a and b). Fifth, the sensitivity of the morphodynamic models to transport relations was tested (van Rijns vs Engelund and Hansen) (Run 5). Finally, we tested the effect of secondary flow to the modelling results (Run 6) by neglecting the secondary flow.

On the basis of the sensitivity analysis, the best parametrizations were selected for the final 2D and 3D models, which were assessed against detailed field measurements of flow and morphology. We used spatially varying grain size, a low factor for transverse bed slope effect (factor = 1), van Rijn's sediment transport relation, and we included the secondary flow correction to the 2D simulation. The varying Manning's roughness and uniform Chezy roughness produced almost equally good results (flow velocity and water level) during the model calibration. However, as model stability suffered slightly from the use of spatially varying Manning's n, we selected a uniform Chezy value of 55 to the final model runs. The 3D model was built simply by adding seven σ-layers to the 2D model so that the final 3D model contained eight vertical layers with the following percentage thicknesses from bottom to top: 9, 13, 17, 22, 17, 11, 7 and 4. Constant horizontal eddy diffusivity ($0.04\,m^2\,s^{-1}$) and viscosity ($0.07\,m^2\,s^{-1}$) were used in both 2D and 3D simulations. In 3D simulation, the 3D turbulence (vertical diffusivity and viscosity) was based on the k–ε turbulence closure model. The water temperature was set to change linearly from 2.7 to 5.4 °C during the modelling period in both simulations. Along closed boundaries, the velocity component perpendicular to the closed boundary was set to zero (a free-slip condition). To determine the erosion of dry cells adjacent to wet cells, we used a scheme that allowed a partial redistribution of the erosion flux from a wet cell so that 50% of the incision in the wet cell is shared with the adjacent dry cells, resulting in incision of the dry cell. For all the simulations, the initial sediment concentrations were set to zero, and after the spin-up time of 300 min, the solution (hydrodynamic and morphodynamic) dependent on the BCs was reached. The actual simulation with morphological updating began 720 min from the start. The sediment calculations were not carried out in cells where the water depth was less than 0.05 m. The modelling results were compared with each other and with field measurements.

The bed shear stress ($N\,m^{-2}$) at the bend apex (Cross-section B) for three flow stages based on the 2D and 3D models was exported from the models (Figure 12). In Delft3D, the bed shear stress is calculated according to following equation:

$$\tau = \frac{g\rho_0 u|u|}{C^2} \tag{30}$$

In 3D simulation, the flow velocity is the horizontal velocity in the first layer just above the bed. In 2D simulation, the magnitude of the depth-averaged velocity is determined from the velocity near the bed, assuming a logarithmic velocity profile. The bed shear stress was calibrated to a water temperature of +5 °C by multiplying the values by following formula:

$$\left(\frac{\mu_5}{\mu}\right)^{\frac{2}{3}} \tag{31}$$

where μ_5 is the viscosity of the water at +5 °C ($1.519 \times 10^{-4}\,Pa\,s^{-1}$) and μ is the viscosity of the water at +25 °C ($8.9 \times 10^{-5}\,Pa\,s^{-1}$).

The modelling results of both 2D and 3D simulations were then compared with each other and assessed against the field measurements of ADCP and MLS.

RESULTS

Sensitivity analyses

The morphological changes predicted by Run 2 (spatially varying grain size) differed most from the default run (Run 1) (Figures 2 and 3). Run 2 predicted the highest point bar top bed level of all the runs (Figure 2). The final channel geometry of Run 2 was also rougher and more irregular compared with the other runs (1–6). Especially, the predicted geometry of the deep areas was irregular compared with other runs that predicted rather smooth final bed topographies. The grain size parametrization particularly affected the predicted geometry of the pools: at the bend entrance (Cross-section A) and apex (Cross-section B), less filling of the pools was predicted by Run 2 compared with other runs with uniform grain size (Figure 4). Run 2 predicted the most deposition on the point bar head, whereas Run 3c (spatially varying Manning) predicted most erosion in the same area (Figure 3). The predicted changes over the point bar by Run 2, and Run 3c differed most from the default run. Run 3a (uniform Chezy) predicted the lowest point bar top elevation, whereas Run 5 (EH transport formula) still predicted the least pronounced vertical bed level variation along the thalweg and the most pronounced filling of the pool beyond the apex (Figure 2). The elevation of the deepest pool, predicted by Run 5, was 12.57 m, whereas by Run 1, it was only 12.17 m. The most important effect of transverse bed slope parametrization to the morphodynamics was also found around the thalweg beyond the apex (Figures 2 and 4). Run 4a (high transverse bed slope effect) predicted more filling of the

DOI: 10.1002/hyp

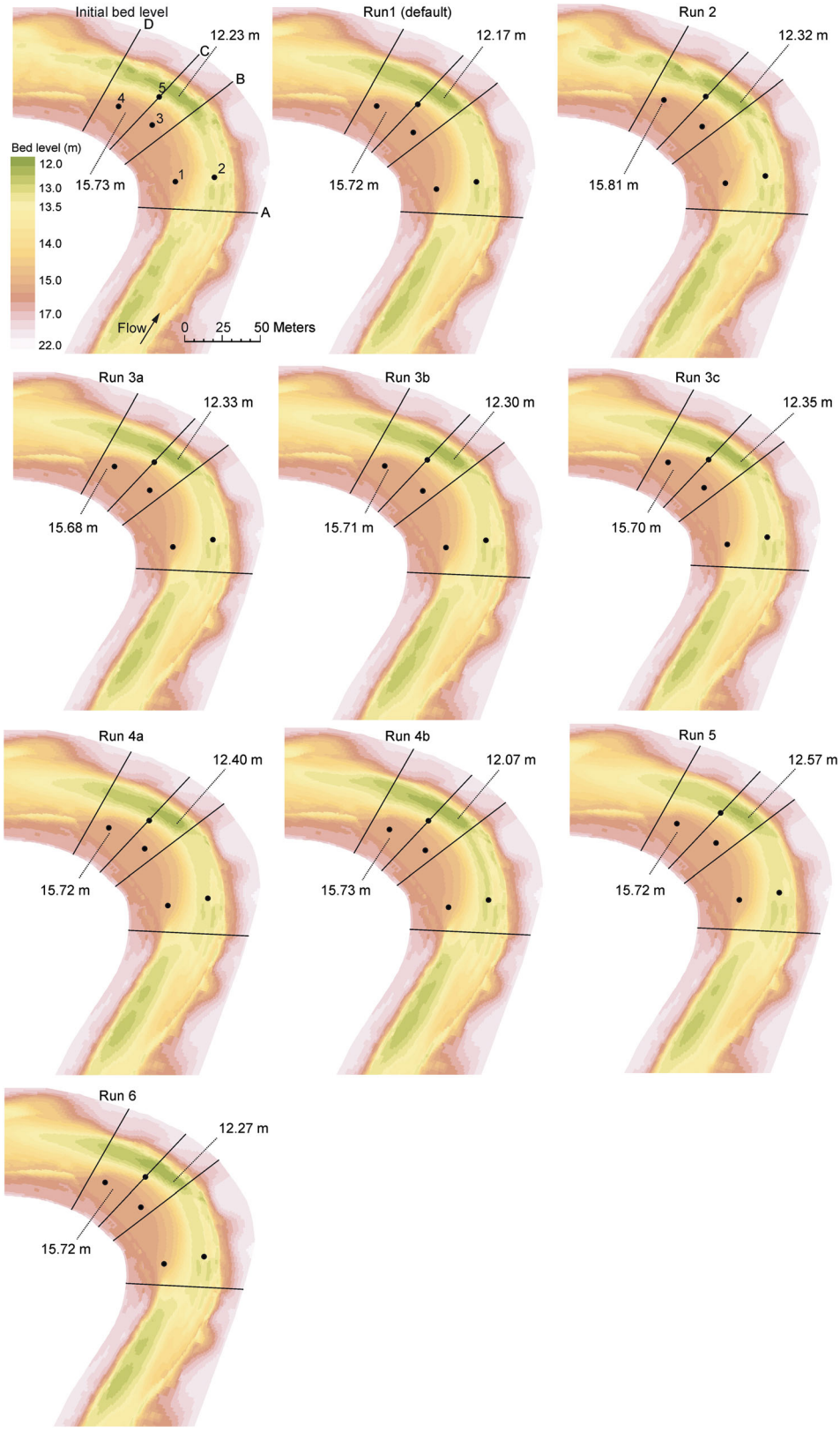

Figure 2. The initial channel geometry and final channel geometries of each run (1–6) of the sensitivity analysis. The elevations of the top of the point bar and the deepest point of the channel are marked in the figure. Cross-sections A–D and observation points 1–5 are marked in the figures

DOI: 10.1002/hyp

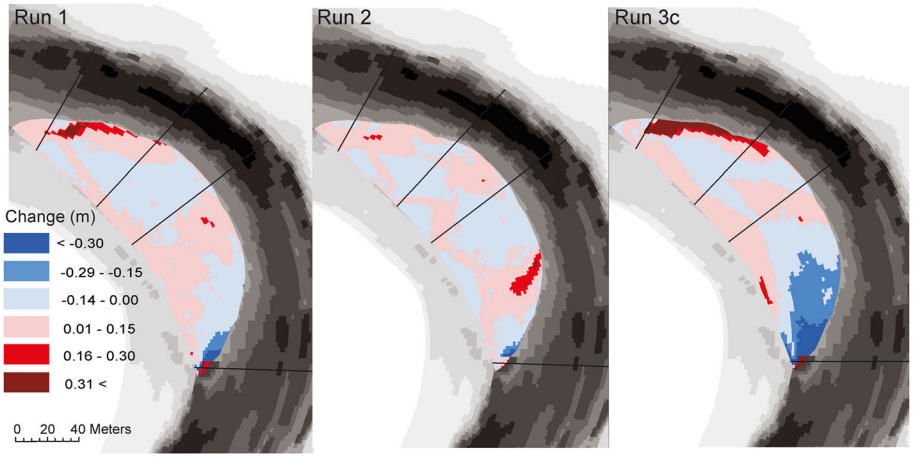

Figure 3. Morphological changes predicted by Runs 1 (default), 2 (spatially varying grain size) and 3c (spatially varying Manning's *n*) of the sensitivity analysis. Cross-sections A–D are marked in the figures

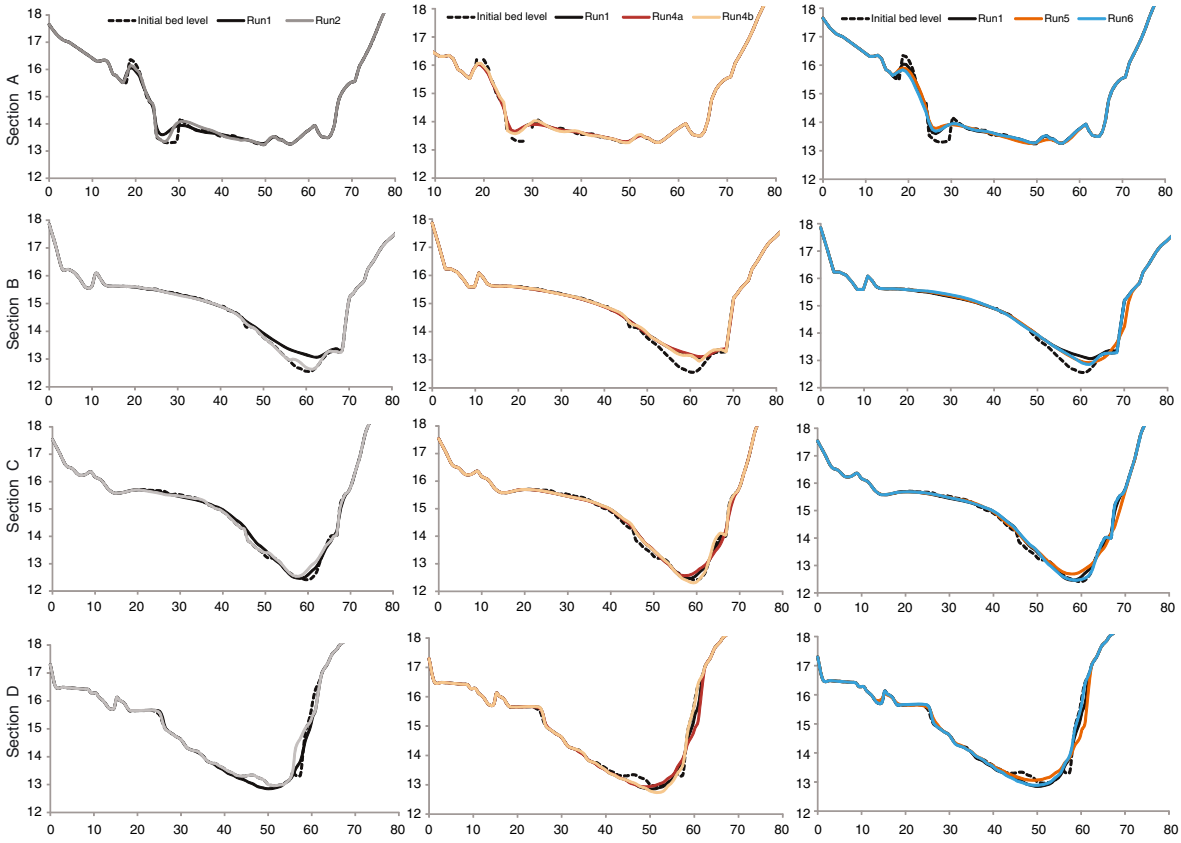

Figure 4. The final channel geometries of the Cross-sections A–C predicted by Runs 1, 2, 4a, 4b, 5 and 6 of the sensitivity analysis

pool beyond the apex compared with Run 4b (no transverse bed slope effect), which predicted the deepest pool of all the model runs (elevation 12.07 m). In addition, Run 4b predicted a more pronounced vertical variation over the longitudinal dune around Point 2 (Figure 2). Compared with the transverse bed slope effect, the grain size parametrization affected more on the geometry of the pool at the bend entrance (Figures 2 and 4). The exclusion of the effect of the secondary flow did not have as much effect on the predicted morphodynamics (Run 6); however, it predicted minor filling of the pool at the thalweg beyond the apex, whereas the default run with secondary flow correction predicted minor erosion in the area (Figure 2).

DOI: 10.1002/hyp

As evident in Figures 2–4, it is confirmed that the parametrization of grain size distribution (Run 2) and the sediment transport relation (Run 5) affected the predicted morphodynamics of the bend. The VR and EH transport relations predicted similar bed level changes at Points 2, 4 and 5, whereas at Point 1, EH predicted more deposition and at Point 3 less erosion compared with the default model run with VR (Figure 5). By contrast, deposition was predicted at Point 3 by Run 2, emphasizing the significance of the grain size parametrization at low flow velocities (the point lies on the top of the point bar). In general, the changes predicted by Run 2 did not consistently follow either the changes of Run 1 or Run 5. At Points 1 and 3 (especially Point 1), which was located in the shallow part of the channel, the changes predicted by Runs 2 and 5 resembled each other largely. However, at Point 3, which was located in the shallowest area of the five points, the predicted changes by Runs 2 and 5 were also much more correspondent compared with Run 1, even though minor deposition was predicted by Run 2, whereas Run 5 predicted minor deposition.

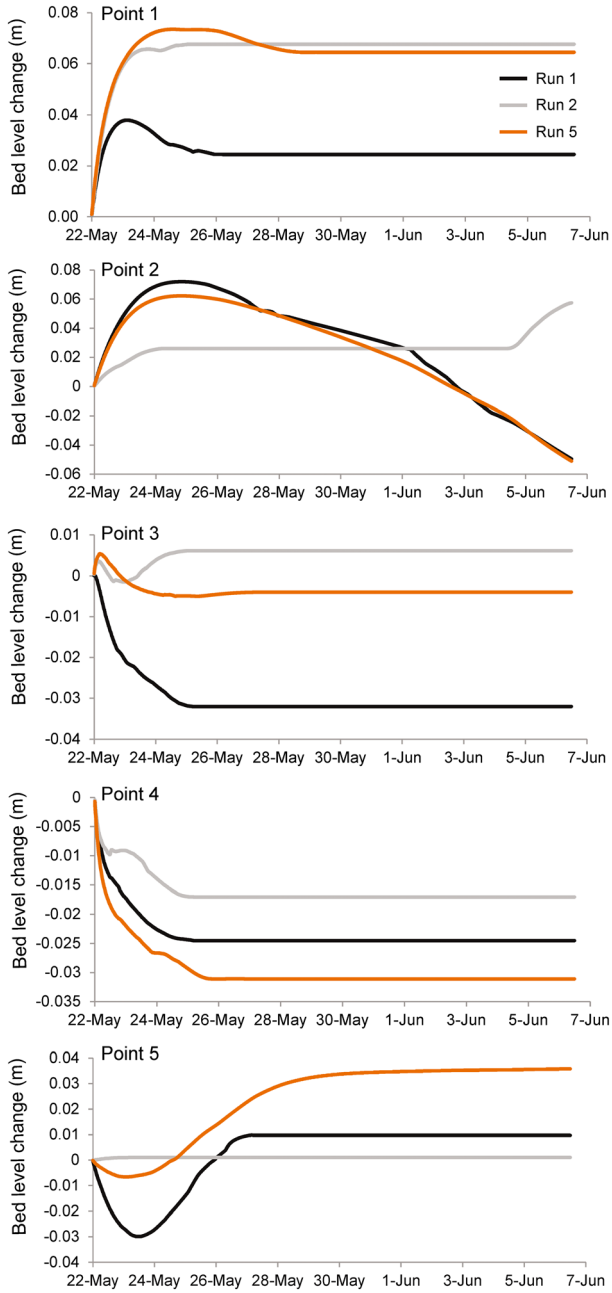

Figure 5. Bed level change at Points 1–5 predicted by Runs 1, 2 and 5. The figure shows the effect of grain size parametrization and the sediment transport relationship on the morphological changes

The sediment transport relation affected the total sediment transport more in high transport rates (=during high discharge) compared the low transport rates (Figure 6). During high discharges, VR predicted higher sediment transport rates compared with EH, whereas during low discharges, EH predicted higher transport rates.

The roughness parametrization affected the distribution of depth-averaged velocity over the river sections (Figure 7). The velocities predicted by spatially varying Manning's n (Run 3c) were most evenly distributed along the river cross-section at the bend apex during both high and low discharges because lower roughness values were located on the point bar compared with the deep areas. On the point bar, the velocities predicted by Run 3a (uniform Chezy) and 3c were higher compared with Runs 1 and 3b (uniforms k_s) during both high and moderate discharges. This was expected as uniform Chezy roughness means a spatially varying k_s and n (smaller values on shallow areas). During moderate discharge, the constant n and k_s predicted unevenly distributed flow velocities along the transect (HVC at the thalweg), whereas constant Chezy and varying Manning resulted on rather evenly distributed velocities. During high discharge, a clear HVC was located on the point bar according to Run 3a (uniform Chezy).

The variation of flood time water levels due to roughness parametrizations was effectively constant (Figure 8). Run 1 predicted highest, Run 3b second highest, Run 3c second lowest and Run 3c the lowest water levels in each point (1–5). The differences in the predicted water levels, thus seem to be a consequence of the parameter values, not the method of parametrization. However, the implications of the velocity and water level variations in the morphological changes are minor: the method of roughness parametrization did not have much effect on the morphodynamic reconstruction of the river bend (Figure 2).

Evaluation of computational reconstructions

During the moderate flow stage, the correlation between the depth-averaged velocities of the 2D and 3D models was 0.99 and 0.68 along Cross-sections A and C,

DOI: 10.1002/hyp

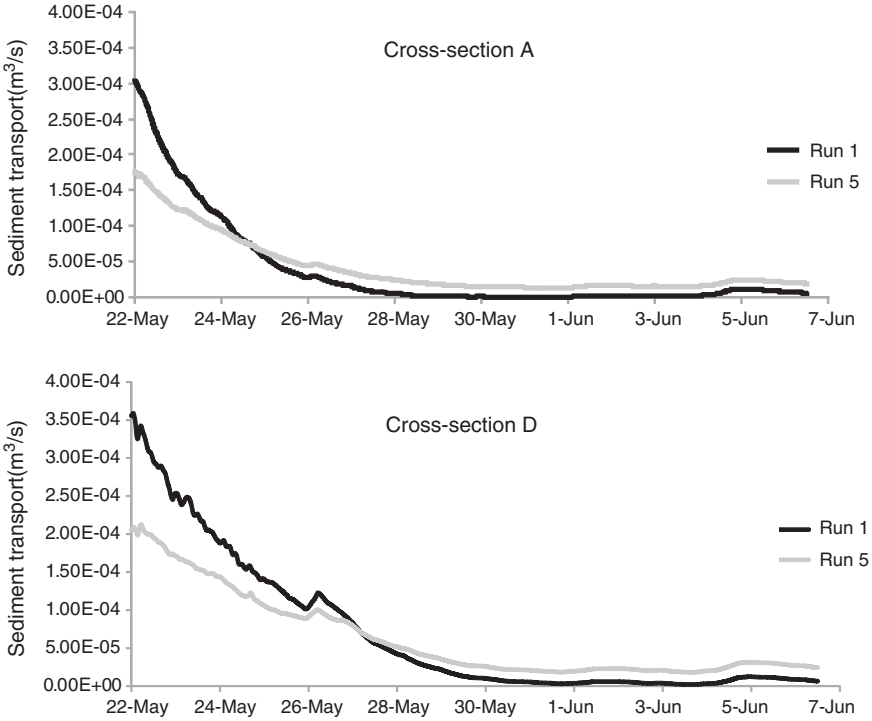

Figure 6. Variation of total sediment transport rate at Cross-section A and D during the entire modelling period predicted by two different transport relationships, that is, van Rijn (Run 1) and Engelund and Hansen (Run 5)

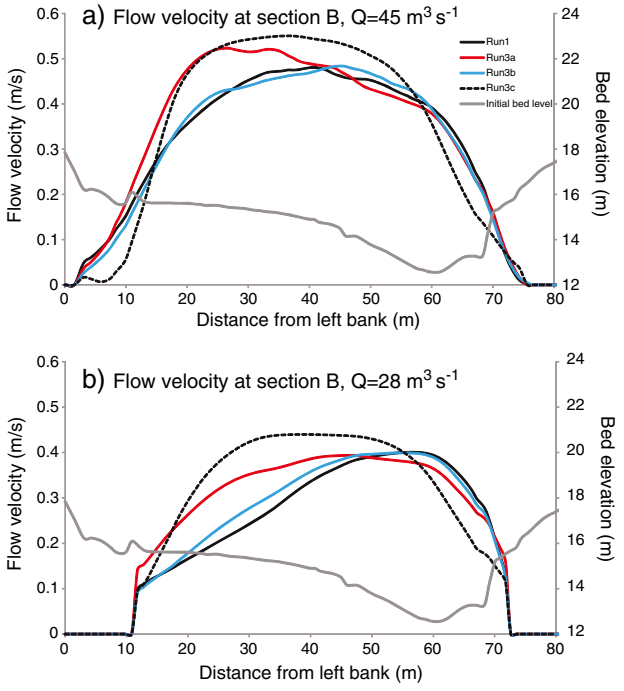

Figure 7. Distribution of depth-averaged flow velocities, along Section B, during high and moderate discharges, showing the effect of roughness parametrization on the flow velocities

respectively (Table III). Along both cross-sections, the modelled and measured depth-averaged velocities varied mostly between 0.2 and 0.5 m s^{-1} (Figure 9a and b). Along Cross-section A, the measured velocities were approximately 0.05 m s^{-1} higher than those modelled, and the correlations between the measured and modelled velocities according to the 2D and 3D models were 0.97 and 0.96, respectively (Figure 9a). Along Cross-section C, there was relatively little variation in the measured and modelled depth-averaged velocities: the standard deviation of the depth-averaged velocity was 0.041, and the differences between the ADCP-based and model-based velocities were less than 0.04 m s^{-1} (Table III, Figure 9b). However, the correlations between the ADCP data and the 2D and 3D model-based data were 0.29 and 0.42, respectively. The highest measured and modelled depth-averaged velocities in Section A were 0.48 and 0.41 m s^{-1}, respectively. The measured HVC was located closer to the inner bank compared with that modelled. On Cross-section C, there were two HVCs in both measured and modelled data, and the highest depth-averaged velocities (0.44–0.46 m s^{-1}) were located on the point bar near the left bank and above the thalweg, ADCP-based values being 0.2–0.4 m s^{-1} higher than the modelled. Thus, the models predicted an increase in the peak velocities beyond the apex, whereas the ADCP data showed that the peak velocities decreased. The depth-averaged flow directions obtained by the 2D and 3D models differed little from each other at Sections A and C (Figure 10). The modelled and measured depth-averaged flow

DOI: 10.1002/hyp

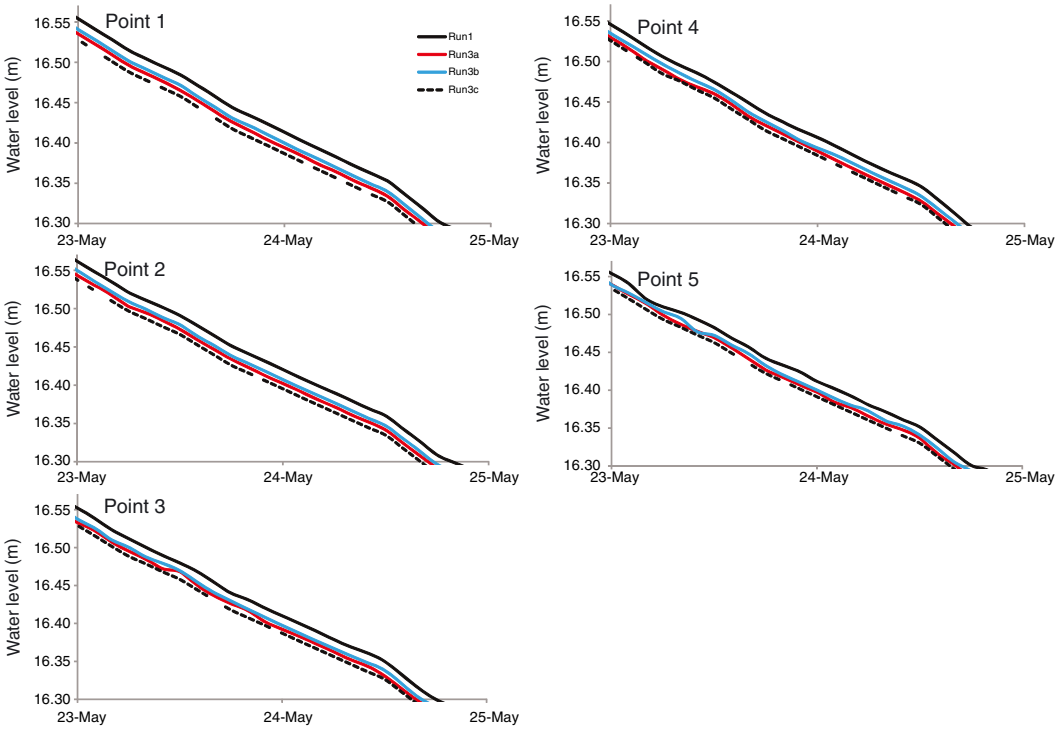

Figure 8. Variation of the water surface elevation during the flood (23 to 25 May) at Points 1–5 predicted by Runs 1, 3a, 3b and 3c. The figure shows the effect of roughness parametrization to the water level changes

Table III. Values describing the modelled and measured flow characteristics and their correspondence during moderate discharge ($28\,m^3\,s^{-1}$) on 26 May (2010). The relative difference is the proportion of the average difference from the ADCP mean velocity. The values are based on the same data as in Figures 2 and 3 ($m\,s^{-1}$)

	Cross-section A	Cross-section C
Correlation coefficient (r)		
Depth-averaged flow (3D model vs ADCP)	0.96	0.42
Depth-averaged flow (2D model vs ADCP)	0.97	0.29
Depth-averaged flow (2D model vs 3D model)	0.99	0.68
Near-bed flow (3D model vs ADCP)	0.91	0.45
Standard deviation		
Depth-averaged velocities (2D, 3D and ADCP)	0.09	0.040
Near-bed flow (3D and ADCP)	0.09	0.093
Average velocity		
Depth-averaged flow (3D model)	0.32	0.40
Depth-averaged flow (2D model)	0.33	0.38
Depth-averaged flow (ADCP)	0.37	0.42
Near-bed flow (3D model)	0.21	0.27
Near-bed flow (ADCP)	0.35	0.42
Average difference		
Depth-averaged flow (3D model vs ADCP)	0.05	0.02
Depth-averaged flow (2D model vs ADCP)	0.05	0.04
Depth-averaged flow (2D model vs 3D model)	0.01	0.02
Near-bed flow (3D model vs ADCP)	0.14	0.15
Relative difference		
Depth-averaged flow (3D model vs ADCP; %)	14	4.9
Depth-averaged flow (2D model vs ADCP; %)	12	8.6
Near-bed flow (3D model vs ADCP; %)	40	36

DOI: 10.1002/hyp

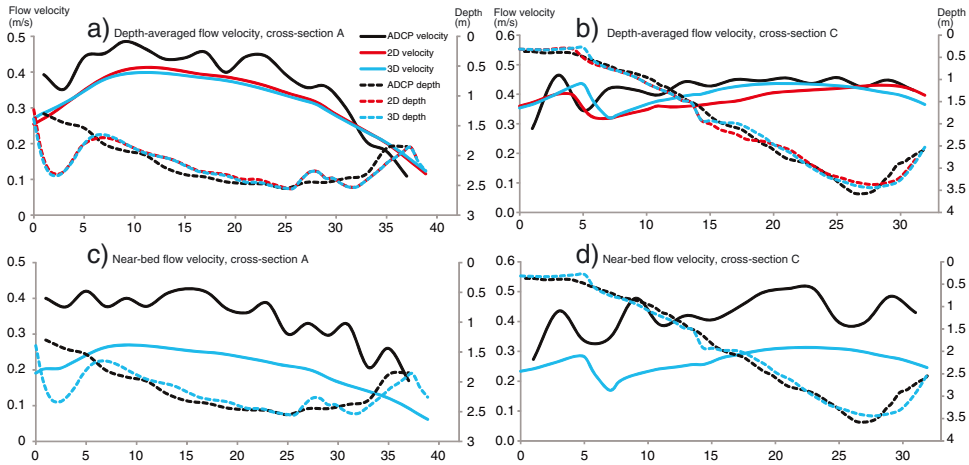

Figure 9. Modelled and measured (ADCP-based) horizontal velocities during moderate discharge (28 $m^3 s^{-1}$) on 26 May: (a,b) depth-averaged flow velocities; (c,d) near-bed flow velocities. The velocity magnitudes are plotted against the distance from left bank (m) along two river sections (A and C), which are shown in Figure 1b. Each velocity value is an average of samples over 2 m. The modelled and measured riverbed profile is visible in the figures. Values describing the datasets are collected in Table III. The flow directions of the same dataset are visualized in Figure 10

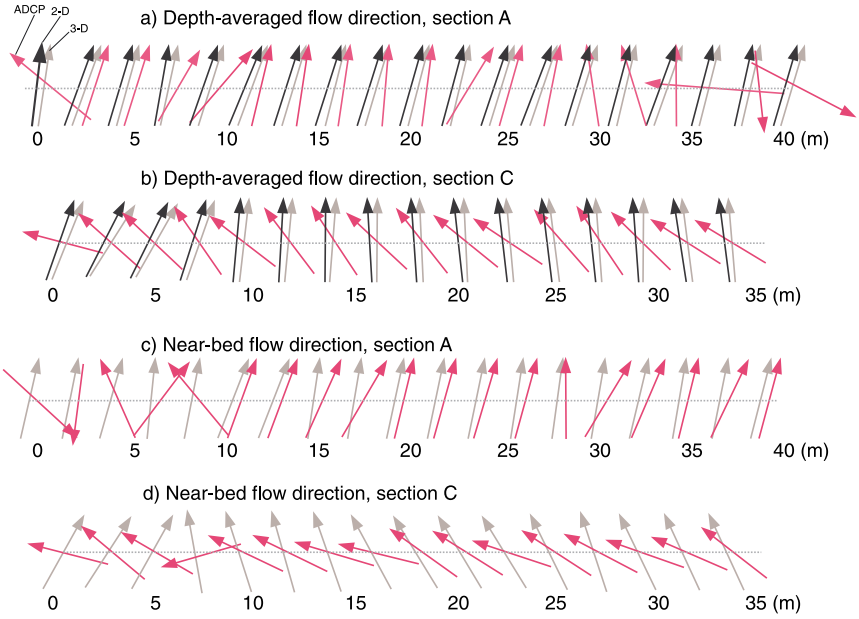

Figure 10. Modelled and measured flow directions along Sections A and C during moderate discharge (28 $m^3 s^{-1}$) on 26 May: (a,b) depth-averaged flow direction; (c,d) near-bed flow direction. The same datasets are used in Table III and Figure 9

directions corresponded rather well along Section A, where the depth-averaged flow was directed slightly towards the outer bank (Figure 10a); however, the ADCP-based flow was irregularly directed near the banks, indicating a helical flow due to the flow–bed interaction. By contrast, the ADCP-based flow was directed towards the inner bank throughout Cross-section C beyond the apex, whereas the modelled flow was directed mostly downstream and also towards the outer bank over the point bar (near the left bank) (Figure 10b).

The measured and modelled near-bed velocities differed more from each other (relative difference 36–40%) compared with the depth-averaged velocities (relative difference 4.9–14%) (Table III). Along Cross-section A, the measured and modelled near-bed velocities were below 0.42 and 0.3 m s^{-1}, respectively, and the correlation was 0.91 (Figure 9c). By the 3D model, the near-bed velocities were ~50–72% and by ADCP 82–110% of the depth-averaged velocities. The average difference between the measured and modelled near-bed velocities was 0.14 and 0.15 m along Sections A and C, respectively. The near-bed velocities, modelled and measured, along both Sections A and C had relatively small standard deviations, that is, 0.09 and 0.093, respectively (Table III). Along Section C, the

DOI: 10.1002/hyp

highest measured near-bed velocity was 0.51 m s^{-1}, and the highest modelled was 0.32 m s^{-1}, and the correlation between the modelled and measured data was 0.45. In both sections, the ADCP near-bed flow velocities were remarkably higher than those modelled. Both the modelled and measured near-bed velocities were directed towards the outer bank along most of the Section A and towards the inner bank along most of the Section C (Figure 10c and d). However, along Section C, the ADCP-based inward flow was more emphasized, and near the inner (left) bank, the model also predicted an inward near-bed flow, which was not evident in ADCP measurement. The proportion of the depth-averaged transverse velocity (i.e. horizontal velocity perpendicular to the main flow) was ~10% of the main flow, whereas the near-bed transverse velocity obtained by the 3D model was only ~5.5% of the depth-averaged main flow.

During high discharge, the flow was directed towards the outer bank at the bend entrance (Section A) according to both measured and 3D model-based cross-sectional data (Figure 11a and b). The outward flow reached almost the entire cross-section according to both measured and modelled data. Only above the point bar was there evidence of an upward flow in both measured and modelled data, and the model showed evidence of flow separation, which was not evident in the ADCP data. In addition, there was downward flow close to the outer bank in both modelled and measured data. The HVC was located slightly towards the inner bank from the thalweg in both cases. The ADCP-based highest velocities were ~0.7 m s^{-1}, whereas the predicted peak velocities were ~0.6 m s^{-1}.

At the bend exit (Section D), the flow was directed towards the inner bank according to the ADCP data throughout the section (Figure 11c). Upward flow was also evident. According to the 3D model, however, the inward and upward flows were located in the deep part of the channel, whereas over the point bar and near the surface, the flow was directed towards the outer bank (Figure 11d). As a matter of fact, the 3D model predicted a secondary circulation of flow with outward flow throughout the water column over the point bar. An inner-bank slow-flow zone was evident in both modelled and measured data at Section D. The HVC was located at the apex in both cases. Thus, its location had shifted towards the outer bank compared with the bend entrance. In addition, the HVC were located closer to the bed at the bend exit compared with the bend entrance. The flow velocities were of the same order of magnitude, the highest velocity being 0.55 m s^{-1} in both modelled and

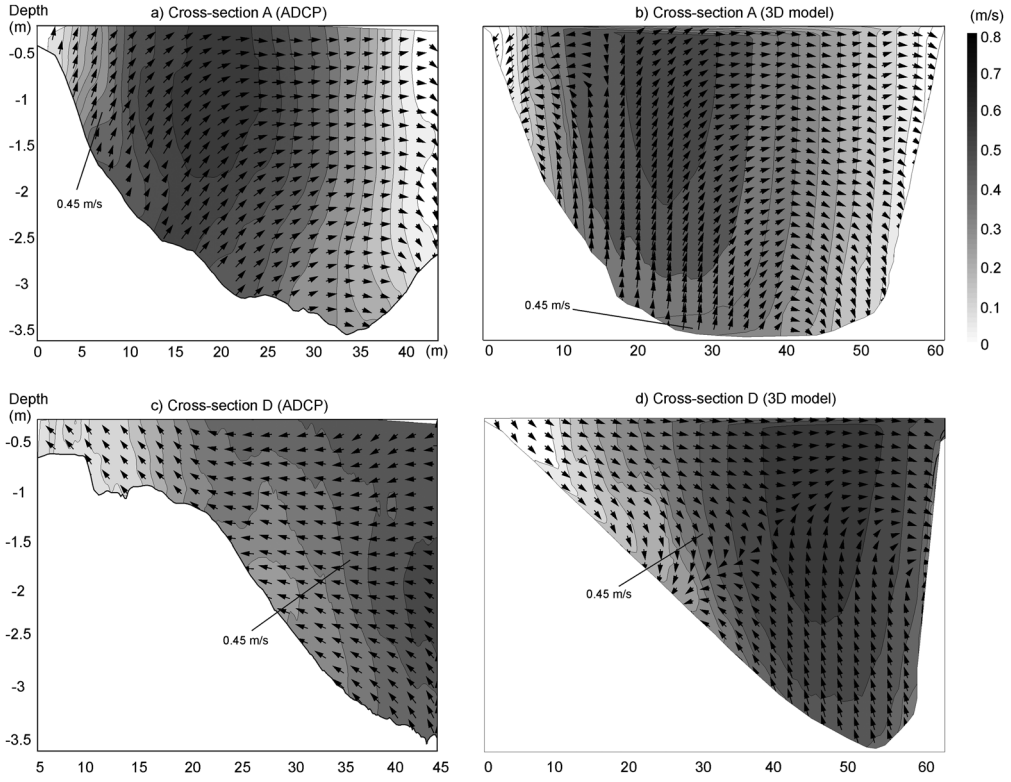

Figure 11. Modelled and measured 3D flow structure during high discharge (45 m^3 s^{-1}) on 22 May: (a) modelled flow field, Cross-section A; (b) measured flow field, Cross-section A; (c) modelled flow field, Cross-section D; (d) measured flow field, Cross-section D. The contours (interval 0.05 m s^{-1}) represent the flow velocities normal to the cross section and arrows the transverse flow velocities. The *x*-axis is the distance from the left bank (m). One velocity class (0.45 m s^{-1}) is marked in each figure for interpretation of the velocity contours

DOI: 10.1002/hyp

measured data. As in Figure 9, the ADCP based highest velocities also decreased beyond the apex here.

There was a notable difference between the modelled near-bed and near-surface velocity magnitudes (Figure 12a and b) even though the depth-averaged velocity magnitudes of both 2D and 3D simulations were rather uniform (Figure 9a and b). The near-bed velocities were lower and the near-surface velocities were higher compared with the 2D model's depth-averaged velocities (Figure 12). The high velocities became submerged as the distance downstream increased: at the downstream end of the bend, the near-bed layer high-velocity zone was expanding, whereas the surface flow velocity was slowing down. According to both simulations, the HVC also shifted towards the outer bank with distance downstream (Figure 12a–c). The 2D model also showed an increase in the highest flow velocities beyond the apex, contradictory to ADCP measurements illustrated in Figures 9 and 11. A zone of recirculation at the inner bank beyond the point bar was evident in all three velocity fields. In addition, a smaller recirculation zone was observed near the outer bank at the bend entrance. The depth-averaged

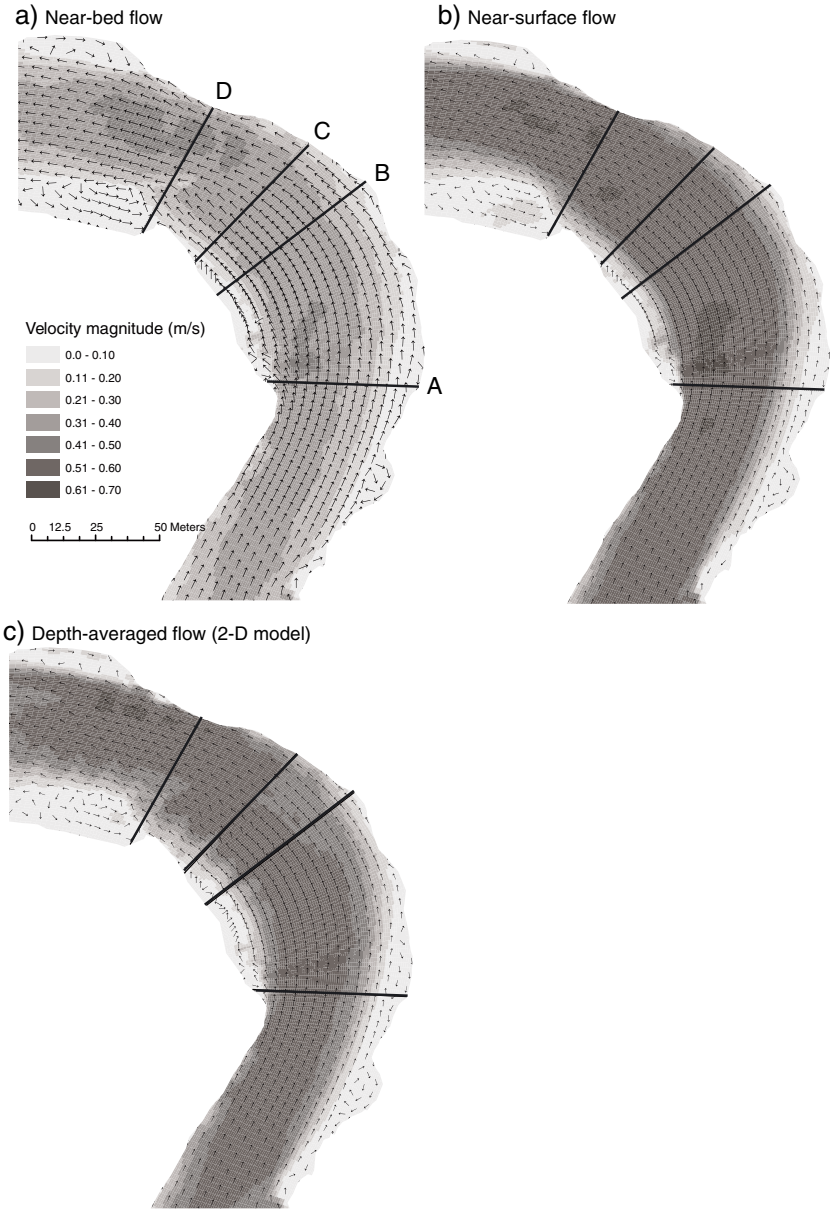

Figure 12. Modelled horizontal velocity magnitude and direction over the AOI during high discharge (45 $m^3 s^{-1}$) on 22 May: (a) near-bed velocity based on the 3D simulation; (b) near-surface velocity based on the 3D simulation; (c) depth-averaged horizontal velocity based on the 2D simulation. The velocity magnitudes are visualised using contours and the direction using arrows. The directions are visualised on every fourth grid point. Cross-sections A–D are marked in the figures

DOI: 10.1002/hyp

model predicted more evident outward flow near the inner bank compared with the 3D model.

Overall, the 3D model resulted in larger bed shear stress values compared with the depth-averaged model (Figure 13). In areas with high bed shear stress, the difference between the models was also larger. The largest bed shear stress was located slightly towards the inner bank from the thalweg during each flow stage according to both models. During high flow, the maximum bed shear stress was located over the point bar. According to the 2D model, the magnitudes of the peak bed shear stress were 0.85, 0.55 and 0.45 $W m^{-2}$ during high, moderate and low discharges, respectively. According to the 3D model, the corresponding values were 1.2, 0.75 and 0.63 $W m^{2}$.

In general, the modelled and measured morphological changes on the point bar were of the same order of magnitude: the measured changes were between –0.41 and 0.41 m, and the modelled changes according to the 2D and 3D models varied between –0.39 and 0.75 m and between –0.40 and 0.73 m, respectively (Figure 14a–c). The changes predicted by the 2D and 3D models were very alike, but they differed somewhat from the measured changes. However, some morphological features were evident in all three cases (E1-2 and D1-3 in Figure 14). Erosion had occurred on the upstream part of the point bar (E1); however, the magnitude of measured erosion was greater than in the simulation results, and the modelled erosional areas were located further upstream compared with those measured. Another erosional area was located on the point bar margin around the apex (E2). The measured erosion was rather minor and located slightly beyond the apex. The models predicted erosion of the same magnitude (<0.2 m), but the area was larger and located further upstream than that measured. Furthermore, there were three depositional areas that were present in both measured and modelled data (D1-3). The depositional areas on the point bar tail (D1 and D2) are typical accumulation areas for point bars. These were predicted reasonably well by both 2D and 3D models. Although there was also a simulated depositional area on the point bar head (D3), the predicted changes over the area were mostly minor (–0.1 to 0.1 m). In reality, deposition of up to 0.4 m had occurred in places and the depositional area dominated almost the whole upstream part of the point bar. The 3D simulation had reproduced a slightly larger depositional area compared with the 2D simulation.

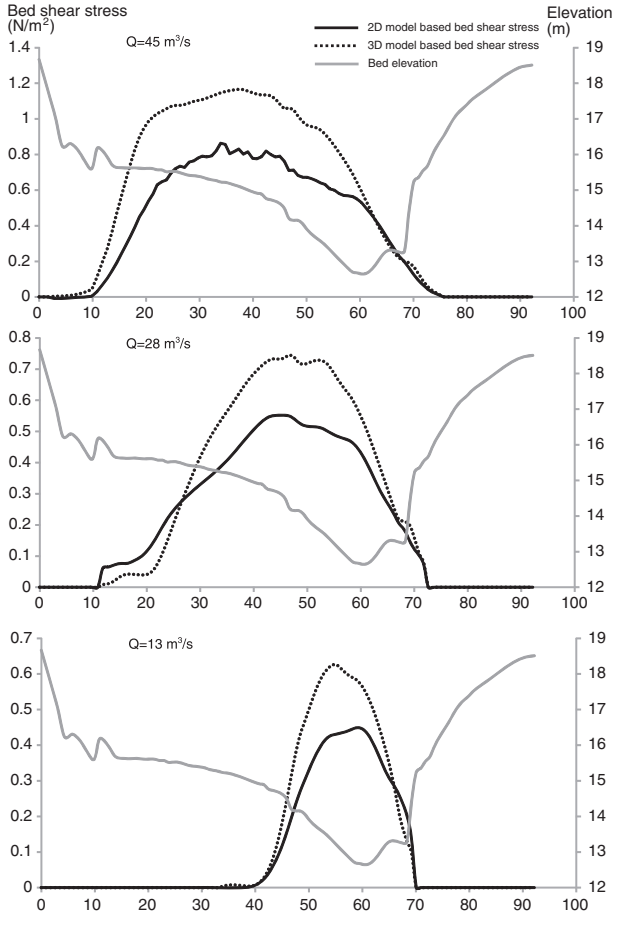

Figure 13. Simulated stream power based on 2D and 3D model at the bend apex (Cross-section B): (a) high discharge (45 $m^3 s^{-1}$) on 22 May; (b) moderate discharge (28 $m^3 s^{-1}$) on 26 May; (c) low discharge (13 $m^3 s^{-1}$) 30 on. The initial bed level along the section is marked in the figure. The *x*-axis represents the distance from the left bank (m). Location of the cross-sections shown in Figure 1

DISCUSSION

This study consists of two parts. In the first part, sensitivity of the 2D hydrodynamic and morphodynamic models to various user-defined modelling parameters was tested. In the second part, 2D and 3D morphodynamic reconstructions were performed over a natural meander bend, and the results were assessed against detailed field measurements.

Sensitivity analysis

In the first part of the study, of all the analysed parameters, the parametrization of grain size distribution affected most on the predicted morphodynamics over the meander bend. The significance of the grain size parametrization was emphasized at low flow velocities, when the threshold velocity of the initiation of motion was not reached for all the particle sizes. The model run with varying D_{50} value of the sediment also predicted bar head deposition, a feature that was not predicted by any other model run and that occurred in reality. This implies that, as the spatial distribution of the grain sizes leads to more notable spatial variation of sediment transport compared with uniform grain size, also, the predicted

DOI: 10.1002/hyp

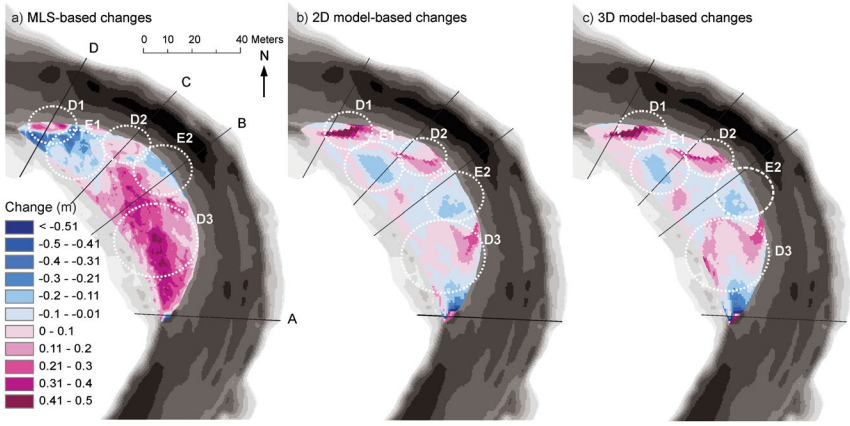

Figure 14. The morphological changes on the point bar caused by the flood event: (a) measured changes based on the multi-temporal MLS-survey; (b) modelled changes based on the 2D simulation; (c) modelled changes based on the 3D simulation. The mean differences between the datasets of changes were as follows: MLS vs 2D model: 0.101 m, MLS vs 3D model: 0.096 m and 2D vs 3D model: 0.004 m. Cross-sections A–D are marked in the figures

morphological changes depend on the grain size parametrization. As the grain size parametrization in this study was based on field measurements of the grain size distribution, it also functioned better than the uniform grain sizes in predicting the morphological changes.

The sensitivity analysis of this study confirmed the request to use spatially varying (physically based) grain size parametrization in morphodynamic models, suggested by many previous studies (e.g. Nicholas, 2000; Nicholas, 2013; Lotsari *et al.*, 2014). Pinto *et al.* (2006) also reported that the van Rijn transport formula is very sensitive to grain size parametrization; however, grain size parametrization requires extensive field investigation, and still, it is not possible to capture fully the actual bed composition of a natural site. Parametrization of the bed composition seems the most challenging part of the morphodynamic simulation. This makes the morphodynamic reconstruction of a natural river far more complicated than a reconstruction in a laboratory environment, at least in environments with high spatial variability in bed material, such as meander bends.

The roughness parametrization affected, as expected, both the simulated hydrodynamic and morphodynamics. On the point bar, the velocities predicted with uniform Chezy or spatially varying (bed composition-based) Manning's n were higher compared with constant Manning's n or Nikurandse k_s. This was expected as uniform Chezy roughness means spatially varying k_s and n (smaller values on shallow areas). Compared with the field measurements, the uniform Chezy and spatially varying Manning's n produced the most accurate flow fields. Thus, in a meandering river environment, a uniform Chezy seems to work well, as there is often less roughness over the high areas, such as on point bar tops. However, the roughness parametrization method had not much effect on the spatial variability of water level. The spatially varying Manning's n (low roughness over the point bar), however, led to the most extensive erosion over the point bar head of all the test runs of the sensitivity analysis. In addition, the uniform Chezy roughness resulted in low point bar height and small pool depth compared with uniform Mannings n, although the difference between the point bar top elevation, modelled using uniform Manning's n and Chezy, was only 0.04 m. The pool was 0.16 m shallower than predicted by constant Manning's n and 10 cm shallower than in the initial channel. This is consistent with the studies of Schuurman *et al.* (2013) and Lesser *et al.* (2004). Schuurman *et al.* (2013) modelled morphological changes in an idealized braiding river environment. In their study, uniform Chezy roughness resulted in shallower channels and lower and smoother bars. Compared with uniform Nikuradse k_s, the Chezy also resulted in lover point bar height and a slightly shallower pool in current study. However, Lesser *et al.* (2004) stated that the uniform Chezy resulted in morphological changes of a curved channel not in line with the experimental results. In the current study, we were not able to compare the predicted geometry of the deep areas with field data.

The transverse bed slope parametrization affected most the morphology of the thalweg beyond the apex. The model run with a high transverse bed slope effect predicted more filling of the pool beyond the apex compared with the model run with no transverse bed slope effect, which predicted the highest pool depth of all the model runs. Contrary to the findings of Schuurman *et al.* (2013) and Nicholas (2013) the effect of bed slope parametrization to the point bar morphology was minor. The difference of the point bar top elevation between model runs with high and no transverse bed slope effect was only 0.01 m; however, as the difference of the pool bottom elevation of the same model runs was as high as 0.33 m, its influence cannot be neglected. In addition, the simulated period in the current study was short and the

DOI: 10.1002/hyp

effect of the transverse bed slope parametrization would possibly be more evident in longer term simulation. Thus, at least the spatial variability of the effect of transverse bed slope parametrization as well as the long term effects to the simulated morphodynamics need further research. In addition, as mentioned by Nicholas (2013), the ratio of bed-load to suspended load influences the importance of the transverse bed slope effect. Thus, the chosen sediment transport relationship might have a notable effect on the transverse bed-load transport, also to the morphodynamics in that sense. The parametrizations thus seem to have a case-sensitive effect on the modelling results, and the combined effects of many various paramaters should be investigated in the future.

According to the sensitivity analysis of this study, the sediment transport relation has a notable effect on the predicted morphodynamics over a meander bend. The sediment transport relation affected the total sediment transport more on high transport rates (=during high discharge) compared with the low transport rates. During high discharges, the VR formula predicted notably higher transport rates, whereas during low discharges, the VR predicted slightly higher transport rates. The reason for the remarkable difference in predicted sediment transport during high discharges may be that the calibration coefficient for the suspended load transport in the van Rijn formula (f_{sus}) was set to 2, and the EH predicts only the bed-load transport. This was also noted by Schuurman *et al.* (2013) who pointed out that the van Rijn formula uses a threshold for sediment mobility, which affects the sediment transport rates in locations of low sediment mobility, for example, on top of bars. They also noted that VR predicted much lower sediment transport rates compared with EH. In the current study, the calibration parameters were adjusted to correct the VR formula to correspond better to the field measurements, and therefore, the relationship of the predicted transport rates of these two formulas is different. The study of Pinto *et al.* (2006) also showed that the van Rijn formula is very sensitive to physical properties such as flow velocity and that the sediment transport is extremely sensitive to velocity close to the threshold of motion, low flow velocities. However, according to the current study, the most notable differences of the morphodynamics predicted by VR and EH are located at the deep parts of the channel: the model run with the EH transport formula predicted the most pronounced filling of the pool beyond the apex of all the model runs. In the current study, however, the predictions of different transport formulas were not compared fully with field measurements, and this subject needs further studying.

The exclusion of the effect of secondary flow did not affect much on the predicted morphodynamics; however, it caused a shallower pool at the thalweg compared with the model run with secondary flow correction. According to the sensitivity analysis, the exclusion of secondary flow had only a minor effect on the point bar morphodynamics. The sensitivity analysis of this study was realized only for short-term hydrodynamic and morphodynamics (one flood event), and hence, the response of the model is strongly dependent on initial conditions. Thus, the results are only applicable in short-term studies, and more investigations are needed to assess the sensitivity of long-term models to these parameters. Especially, the parametrization of secondary flow and transverse bed slope in long-term simulations of channel evolution needs further research.

Assessment of the 2D and 3D hydrodynamic and morphodynamic models

In the second part of this study, we compared the results of 2D and 3D hydrodynamic and morphodynamic reconstructions of a meander bend with detailed field observations (multi-temporal ADCP and MLS). In general, the measured and modelled flow velocities and morphological changes were of the same order of magnitude. For hydrodynamics, the 3D model was superior in its ability to model vertical flow, which is always present in a meander bend. In addition, the differences in the modelled bed shear stress show clearly how depth averaging affects the erosional power of the flow, even though Delft3D estimates the near-bed flow velocity of the depth-averaged model assuming a logarithmic velocity profile: depth-averaged simulation resulted in lower bed shear stress values compared with the 3D model. The 3D model also worked slightly better compared with the 2D model in the morphodynamic reconstruction. The 2D and 3D model-based depth-averaged velocities were more similar at the bend entrance ($r = 0.99$) compared with bend exit ($r = 0.68$) during the moderate discharge. On the basis of the model validation of this study and taking into account the significantly higher computational needs of the 3D model, one should consider whether the 3D model is really needed for a particular modelling target.

The measured and modelled depth-averaged velocities at the bend entrance corresponded well for $r > 0.96$. The average differences between the ADCP-based and modelled depth-averaged velocities were $0.05\,m\,s^{-1}$ for both the 2D and 3D models. At the bend exit, the average differences were less than $0.04\,m\,s^{-1}$. According to a sensitivity analysis by Pinto *et al.* (2006), hydrodynamic simulations should be calibrated to within 10% errors in the velocity, and it is preferable to underestimate than to overestimate the flow velocities to avoid errors in the predicted sediment transport fluxes. In the current study, not all the modelled velocities were within 10%

DOI: 10.1002/hyp

difference of the ADCP measurements. The models also predicted that peak flow velocities would increase, whereas according to the ADCP measurements, the peak flow velocities were decreasing beyond the apex. Lotsari *et al.* (online) measured the flow field using ADCP in various flow situations in the same river reach as the current study. In their study, the HVC of depth-averaged velocities had, on many occasions, greater velocities upstream of the apex compared with downstream. This result, based on various measurements, suggests that even though the models simulate the HVC's velocities to increase beyond the apex, the comparisons with advanced flow measurements may prove that developments are needed in models to simulate the flow velocity distribution correctly in meandering river reaches.

The relative difference in the measured and modelled depth-averaged velocities varied between 4.9 and 14% and the correlation between 0.29 and 0.97. On the basis of previous studies of model validation using field data, the results of the velocity comparisons of this study seem typical, and many previous studies have shown problems in quantitative estimations of characteristics (Hodkinson and Ferguson, 1998; Rodriguez *et al.*, 2004; Nicholas *et al.*, 2012). Hodkinson and Ferguson (1998) compared their 3D model results with field measurements of an electromagnetic current meter (ECM), and the correlation between the measured and modelled velocities was 0.94–0.96 ms^{-1}. However, the velocity was also under-simulated in their study, in some sections. Two-dimensional morphodynamic simulations by Lotsari *et al.* (2014) in a braided river also showed that, especially at times of low flow, the depth-averaged simulation results under-predicted the velocities compared with the ADCP measurements. Nicholas and Smith (1999) reached a correlation of 0.88 and a mean difference of 0.09 $m\,s^{-1}$ between the measured and modelled velocities in a meander bend. They only compared the modelling results with 2D field data. Lane *et al.* (1999) reported a correlation of 0.71 for the downstream velocity. In the current study, the correlation between the measured and modelled depth-averaged velocities beyond the apex was only ~0.3–0.4. On the other hand, the difference between the modelled and measured velocity values on the area was small (average differences $<0.04\,m\,s^{-1}$, <8.6% of the measured mean velocity), and the deviation was only 0.04. Thus, the correlation coefficient does not tell much about the modelling performance. The 3D model did not predict the depth-averaged velocities better than the 2D model.

Even though the depth-averaged velocity magnitudes were predicted relatively well at the sections beyond the apex, the measured and modelled flow directions differed notably during both high and moderate discharge. ADCP-based measurements showed that the flow was directed strongly towards the inner bank throughout the water column, whereas the model prediction showed clear evidence of secondary circulation, near-bed inward and near surface outward flow. Even though the ADCP does not measure near the bed or the water surface, it seems unlikely that a full circulation cell existed in nature; instead, it was limited to outward flow at the bend entrance and inward flow at the bend exit. The near-bed flow was directed inward in both datasets, even though the ADCP-based near-bed inward flow was more pronounced and the model predicted outward flow near the inner bank. This outward flow is part of a recirculation zone, which both 2D and 3D models predicted at the inner bank beyond the apex. As the ADCP data showed strong inward flow near the inner bank beyond the apex, it can be assumed that some kind of circulation also existed in nature; however, the recirculation appears, according to the models, close to the bank on a very shallow area, which was unable to access with the ADCP. According to both 2D and 3D models and MLS measurements, deposition had occurred in the downstream part of the point bar margin, indicating classical flow-sediment interaction over the bar tail (Frothingham and Rhoads, 2003; Kleinhans and van den Berg, 2011; Kasvi *et al.*, 2013b).

The flow directions were modelled well at the bend entrance during high and moderate flow. Despite the differences in the bend exit flow directions, evidence of secondary circulation was present in the bend according to both the ADCP and the 3D model: at the bend entrance, there was outward flow in most of the section, apart from the outer bank, where the flow was directed downwards, as in many previous studies (e.g. Bridge and Jarvis, 1982). Beyond the apex, the flow was directed towards the inner bank with upward flow throughout most of the section according to ADCP. In the simulation results, the upward flow was more evident, and it did not cover the point bar. Thus, as also shown by Dargahi (2004), the secondary circulation over a meander bend can be reconstructed with a 3D computational model. The correct flow directions along a natural river bend, however, seem a challenging task and needs further research in model validation.

The location and shift of the HVC were correctly modelled during high and moderate discharges by both 2D and 3D models compared with the ADCP measurements. According to previous studies, the HVC is situated near the convex bank at the entrance of a meander bend and shifts towards the outer bank with distance downstream (Dietrich *et al.*, 1979). The lateral shift of the HVC toward the outer bank with distance downstream was evident also in the measured and modelled data of the current study. This change in HVC location has also been shown recently by Lotsari *et al.* (online) in the same meandering river channel in which the present study was performed.

DOI: 10.1002/hyp

Although the 2D and 3D models predicted equal depth-averaged velocities similarly to the study of Lane *et al.* (1999), the 2D model is not capable of modelling the 3D flow structures present in a meander bend. Rodriguez *et al.* (2004) reported that complex flow structures such as transverse velocity components, helical flow, the recirculation zone and the submergence of a HVC were evident only in the 3D model. The vertical location of the HVC was naturally observable only in the 3D model's results. Both the ADCP-based and 3D model-based near-bed velocities were higher beyond the apex compared with the bend entrance, indicating a vertical shift of the HVC towards the riverbed with distance downstream.

The near-bed flow characteristics are also modelled only in the 3D model. In the current study, the measured near-bed velocities were, however, approximately $0.15\,\mathrm{m\,s^{-1}}$ higher than those modelled, both at the bend entrance and bend exit. As the ADCP device do not measure closer than ~0.25 m to the riverbed, the ADCP near-bed velocities do not represent the real near-bed values, but rather the values 0.25 m above the riverbed. Near the fixed boundaries, the measurement errors are also larger as a result of the flow disturbance caused by the flow–boundary interaction (Nystrom *et al.*, 2007). Nystrom *et al.* (2007) noticed that errors in the measured ADCP velocities were larger in places with high turbulence intensity. Thus, the actual difference between modelled and measured data may not be as big, but another measurement technique, such as an ECM, could be used to measure the flow velocity closer to the bed. Further studies are therefore needed to validate the near-bed flow field of the 3D model.

In general, the differences between the modelled and measured flow magnitudes were mostly random, apart from the fact that the model predicted lower velocities compared with the ADCP. According to Nicholas and Smith (1999), the random differences may reflect a number of factors including sub-grid-scale natural spatial variability in flow velocities associated with local bed structures and, on the other hand, measurement uncertainty resulting from field-based flow measurements. Dargahi (2004) also pointed out that, in the validation process of a hydrodynamic model, inaccuracies in the location of measuring points and velocity measurements may cause errors. As the moving-vessel ADCP measurement is only a snapshot of the flow field of a certain moment, there is a chance that the measured flow field does not represent the dominating flow velocity and direction of that area at that specific flow stage (Szupiany *et al.*, 2007; Muste *et al.*, 2004; Claude *et al.*, 2014).

Because of these noted problems related to the moving-vessel ADCP measurements, other flow measurement techniques should be tested in further studies to ensure the correctness of the field measurements and thus to attain a more reliable validation. ECM cannot be used in deep areas, however (e.g. Hodkinson and Ferguson, 1998), and it takes a great deal of time to take the measurement, a problem also present in fixed-vessel ADCP measurement. Both measurement approaches also disturb the riverbed during measurement because attachment to the bed is needed. Because of these reasons, the moving vessel ADCP measurements were used in the current study.

The morphodynamic reconstruction was assessed against field data only over the point bar, where data with sufficient quality was available. The morphodynamic reconstruction over the bar head did not function as well as that over the bar tail. This was somewhat contradictory to the hydrodynamic reconstruction, which functioned better at the bend entrance, especially direction-wise. According to both simulations, upstream of the apex, most deposition was predicted on the point bar margin and the deposition on the point bar platform was only minor (<0.1 m). According to the MLS change detection, however, deposition dominated the bar head platform completely. Typically, the upstream part of the point bar experiences scour because of high flow velocities and outward flow enhanced with gravitational power (e.g. Bridge and Jarvis, 1976; Dietrich and Smith, 1984). In our study, both the ADCP and 3D models showed clear evidence of outward flow and HVC over the point bar head. However, Kasvi *et al.* (2013a) found that the point bar head may experience marked deposition during moderate flows, despite the high stream power during the flood, because the grain size distribution caused by past flood events (e.g. armour layer) prevents erosion. The scour may thus remain minor, and deposition may dominate the area. This deduction also makes sense in this case study. The sensitivity analysis of this study also showed that with uniform grain size, no deposition was predicted over the bar head. This also proves that a spatially varying (field measurement based) grain size distribution data is necessary in morphodynamic reconstructions of natural river channels. Even though the initial grain size distribution of the models was based on dense sampling on the AOI, the composition of the bed sediment and the composition and amount of the sediment from upstream cause irregularities in sediment transport, which makes the correct modelling of morphological changes demanding (Batalla, 1997).

Generally, a 3D model is considered superior to 2D in hydraulic applications (e.g. Lane *et al.*, 1999; van Maren, 2007). In this study, however, the 2D and 3D models produced remarkably similar morphodynamic reconstructions of the meander point bar, which indicates that the morphodynamics were based mainly on the main flow field. This also confirms the results of previous studies by Duan and Julien (2010) and Rüther and Olsen (2007), according to which the 2D model is able to model the meander migration. The comparison of the measured and

DOI: 10.1002/hyp

modelled morphodynamic models showed that even though some textbook examples of changes were evident in all datasets, the point bar also experienced changes of magnitudes that were not achieved by the models. As the accuracy of the sediment transport formulae is generally considered poor, the calibration and validation of the morphodynamic model is essential (e.g., van Rijn, 1984a; Barry *et al.*, 2004). Calibration is demanding, however, because of errors related to bed-load transport rate measurements in the field (e.g. Ryan and Porth, 1999; Kleinhans and Brinke, 2001). In addition, the bed-load transport rate does not depend only on the flow conditions; for example, the grain sorting, vegetation, run-off, upstream sediment supply, and bed sediment composition affect the magnitude of the sediment transport. Verhaar *et al.* (2008) suggested that the best test for the accuracy of the transport rate predictions would be against inverse morphological estimates from re-surveys of the rivers. Previous studies, in which morphodynamic models have been validated against measured morphological changes, have been performed at lower resolution than the current study, which makes comparison of the results difficult. Dargahi (2004) validated his results with three cross-sectional measurements and reported that the changes were small and thus difficult to measure. Lotsari *et al.* (2014), on the other hand, modelled the macro-form changes and magnitudes with relatively good correspondence in a braided river using a 2D morphodynamic model. However, they simulated a much larger area (5 km) and used a coarser grid (10×10 m) compared with our study. Darby *et al.* (2002) simulated 6 years of morphological changes along a meandering river with cohesive bed material. They compared the modelled results with measured cross-sections. The model predicted the macro-scale changes relatively well, but specific features such as bed slopes and pools were not adequately modelled. In this study, we performed a unique field-based comparison of the measured and modelled sub-bend scale morphological changes on a meander point bar with a very high spatial resolution. The results of our study, combined with previous attempts to model the morphological changes in natural environments, suggest that even though the hydrodynamics could be simulated with relatively high reliability using a 3D model, the detailed morphodynamic modelling of sub-bend scale processes in short temporal scale has major uncertainties. Despite high-quality field measurements and calibration of the sediment transport rates, the results should be treated with caution as many user-defined parameters affect the predicted hydrodynamic and morphodynamics. Thus, as noted by other researchers, more investigation is needed to understand a sufficient amount of calibration and validation data (e.g. Papanicolaou *et al.*, 2008) and to understand the effects of various user-defined parameters on the simulation results in particular circumstances (Schuurman *et al.*, 2013).

CONCLUSIONS

We have presented a unique assessment of the sensitivity and functionality of hydrodynamic and morphodynamic models in a sandy-bed river bend. On the basis of the sensitivity analysis and model validation with multi-temporal MLS and ADCP data, the following conclusions can be drawn:

- The grain size parametrization, transverse bed slope effect and sediment transport relation are critical to the simulated meander bend morphodynamics, the parametrization of grain size distribution having the most pronounced effect. The exclusion of secondary flow had only a minor effect on the point bar morphodynamics.
- The roughness parametrization method affects the spatial distribution of flow velocities but not water level in the hydrodynamic model. For morphodynamics, the uniform Chezy roughness causes low point bar height and small pool depth compared with other roughness parametrization methods.
- The chosen sediment transport relation might change the impact of the other parameters (such as secondary flow and transverse bed slope effect) to the predicted morphodynamics as the modelling of the bed-load and suspended load transport varies between the transport relations.
- A 3D hydrodynamic model should be preferred when investigating the flow characteristics in a meander bend. Although the 2D model reconstructs the depth-averaged flow field satisfactorily, many flow characteristics are lost because of depth averaging: hydrodynamic features, such as secondary flow and vertical location of the HVC, can only be simulated with a 3D model.
- Depth averaging has a significant effect on the erosional power of the flow (e.g. bed shear stress). Depending on the method, according to which the velocity of the depth-averaged simulation is defined for the bed shear stress calculation, the 2D model may result in lower (like in this study) or higher (e.g. in case of using depth-averaged flow velocity) bed shear stress values compared with the 3D model.
- When performing a morphodynamic reconstruction of a meander bend, the superiority of the 3D model compared with the 2D model is not evident. In this study, the 2D and 3D morphodynamic reconstructions of the flood-based changes on a point bar were remarkably similar to each other, and the same morphological units were evident in both models. This also shows that the main flow plays a major role in the simulated morphodynamics, even in a curved channel.

DOI: 10.1002/hyp

- On a short temporal scale, many processes in a meander bend are still beyond the simulation abilities of a computational model. In this study, the model simulated fully developed secondary circulation, which was not evident in the ADCP data. The textbook examples of morphological changes over the point bar were simulated relatively well, but the more unique morphodynamic features were not as evident in the modelling results despite the dense sampling of initial bed sediment sizes and model calibration with bed-load transport rate. This suggests that bed sediment composition (e.g. armour layer), supply and amount, as well as vegetation and run-off, affect the morphodynamics in ways that cannot be simulated without measured data. Thus, morphodynamic modelling should not be used as the main approach when investigating sub-bend scale processes and formations on a short temporal scale.

The sensitivity analysis in this study was only an introduction to increase the understanding of the impact of various user-defined parameters on the simulation results. The findings of this study apply to short-term morphodynamic models and should not be directly applied to models of long-term bend evolution. In the future, the combined effects of various parameters and the spatial variability of their impacts over a river bend should be studied. In addition, the sensitivity of longer term morphodynamic models to various user-defined parameters should be investigated In addition, more specific analysis of the weaknesses and strengths of the models in different sections of the river reach, with particular morphological and hydrodynamic characteristics, is required. The calibration and validation data should be improved: the correctness of the flow measurement should be ensured to be able to identify the causes of the mismatch between measured and modelled data. Higher temporal resolution in topographical comparisons and more advanced sediment transport measurements in higher spatial and temporal resolution would allow for a high-quality calibration and thus improve the morphodynamic modelling ability and evaluation. In addition, the role of the armour layers and bed sediment composition in the short-term modelling results should be studied.

ACKNOWLEDGEMENTS

This study was funded by the Academy of Finland (RivCHANGE), TEKES (GIFLOOD), the Maj and Tor Nessling Foundation (FLOODAWARE), the University of Turku Graduate School and the VALUE Doctoral Programme in Integrated Catchment and Water Resource Management. The fieldwork was carried out with the assistance of Mr Claude Flener, Ms Kristiina Hakkala and Mr Ossi Karvonen.

REFERENCES

Alho P, Mäkinen J. 2010. Hydraulic parameter estimations of a 2D model validated with sedimentological findings in the point-bar environment. *Hydrological Processes* **24**: 2578–2593. DOI: 10.1002/hyp.7671.

Alho P, Baker V, Smith LN. 2010. Paleohydraulic reconstruction of the largest Glacial Lake Missoula draining(s). *Quaternary Science Reviews* **29**: 3067–3078. DOI: 10.1016/j.quascirev.2010.07.015.

Barry JJ, Buffington JM, King JG. 2004. A general power equation for predicting bed load transport rates in gravel bed rivers. *Water Resources Research* **40**: W10401. DOI: 10.1029/2004WR003190.

Batalla JR. 1997. Evaluating bed-material transport equations using field measurements in a sandy gravel-bed stream, Arbúcies River, NE Spain. *Earth Surface Processes and Landforms* **22**: 121–130. DOI: 10.1002/(SICI)1096-9837(199702)22:2<121::AID-ESP671>3.0.CO;2-7.

Bates PD. 2004. Remote sensing and flood inundation modelling. *Hydrological Processes* **18**: 2593–2597. DOI: 10.1002/hyp.5649.

Bates PD, Anderson MG. 2001. Validation of hydraulic models. In *Model Validation: Perspectives in Hydrological Science*, Anderson MG, Bates PD (eds). Wiley: Chichester; 325–356.

Bates PD, Anderson MG, Horritt M. 1998. Terrain information in geomorphological models: stability, resolution and sensitivity. In *Landform Monitoring, Modelling and Analysis*, Lane SN, Richards KS, Chandler JH (eds). Wiley: Chichester; 279–309.

Blizard CR, Wohl EE. 1998. Relationships between hydraulic variables and bedload transport in a subalpine channel, Colorado Rocky Mountains, U.S.A. *Geomorphology* **22**: 359–371. DOI: 10.1016/S0169-555X(97)00055-X.

Bridge JS. 1992. A revised model for water flow, sediment transport, bed topography and grain size sorting in natural river bends. *Water Resources Research* **28**: 999–1013. DOI: 10.1029/91WR03088.

Bridge JS, Jarvis J. 1976. Flow and sedimentary processes in the meandering river South Esk, Glen Clova, Scotland. *Earth Surface Processes and Landforms* **1**: 303–336. DOI: 10.1002/esp.3290010402.

Bridge JS, Jarvis J. 1982. The dynamics of a river bend: a study in flow and sedimentary processes. *Sedimentology* **29**: 499–541. DOI: 10.1111/j.1365-3091.1982.tb01732.x.

Carling P, Villaneuva I, Herget J, Wright N, Borodavko P, Morvan H. 2010. Unsteady 1D and 2D models with ice dam break for Quaternary megaflood, Altai Mountains, southern Siberia. *Global Planetary Change* **70**: 24–34. DOI: 10.1016/j.gloplacha.2009.11.005.

Claude N, Rodrigues S, Bustikko V, Bréhéret J-G, Tassi P, Jugé P. 2014. Interactions between flow structure and morphodynamic of bars in a channel expansion/contraction, Loire River, France. *Water Resources Research*, accepted article. DOI: 10.1002/2013WR015182.

Darby SE, Alabyan AM, Van de Wiel MJ. 2002. Numerical simulation of bank erosion and channel migration in meandering rivers. *Water Resources Research* **38**: 2–21. DOI: 10.1029/2001WR000602.

Dargahi B. 2004. Three-dimensional flow modelling and sediment transport in the River Klarälven. *Earth Surface Processes and Landforms* **29**: 821–852. DOI: 10.1002/esp.1071.

Delft3D-FLOW. 2011. Simulation of multi-dimensional hydrodynamic flows and transport phenomena, including sediments. User Manual. Hydro-Morphodynamics, Version: 3.15, Revision: 18392, 7 September 2011.

Dietrich WD, Smith JD. 1984. Bed load transport in a river meander. *Water Resources Research* **20**: 1355-1380. DOI: 10.1029/WR020i010p01355.

Dietrich WE, Smith JD. 1983. Influence of the point bar on flow through curved channels. *Water Resources Research* **19**: 1173–1192. DOI: 10.1029/WR019i005p01173.

Dietrich WE, Smith JD, Dunne T. 1979. Flow and sediment transport in a sand bedded meander. *Journal of Geology* **87**: 305–315.

Duan JG, Julien PY. 2010. Numerical simulation of meandering evolution. *Journal of Hydrology* **1/2**: 34–46. DOI: 10.1016/j.jhydrol.2010.07.005.

Engelund F, Hansen E. 1967. *A Monograph on Sediment Transport in Alluvial Streams*. Teknisk Forlag: Copenhagen.

Flener CM, Vaaja M, Jaakkola A, Krooks A, Kaartinen H, Kukko A, Kasvi E, Hyyppä H, Hyyppä J, Alho P. 2013. Seamless Mapping of River Channels at High Resolution Using Mobile LiDAR and UAV-Photography. *Remote Sensing* **5**: 6382–6407. DOI: 10.3390/rs5126382.

Frothingham KM, Rhoads BL. 2003. Three-dimensional flow structure and channel change in an asymmetrical compound meander loop, Embarras River, Illinois. *Earth Surface Processes and Landforms* **28**: 625–644. DOI: 10.1002/esp.471.

Hardy RJ, Lane SN, Ferguson RI, Parsons DR. 2003. Assessing the credibility of a series of computational fluid dynamic simulations of open channel flow. *Hydrological Processes* **17**: 1539–1560. DOI: 10.1002/hyp.1198.

Hodkinson A, Ferguson RI. 1998. Numerical modelling of separated flow in river bends: Model testing and experimental investigation of geometric controls on the extent of flow separation at the concave bank. *Hydrological Processes* **12**: 1323–1338. DOI: 10.1002/(SICI)1099-1085(19980630)12:8<1323::AID-HYP617>3.0.CO;2-S.

Hooke JM, Gautier E, Zolezzi G. 2011. River meander dynamics: developments in modelling and empirical analyses. *Earth Surface Processes and Landforms* **36**: 1550–1553. DOI: 10.1002/esp.2185.

Hooke RLB. 1975. Distribution of sediment transport and shear stress in a meander bend. *Journal of Geology* **83**: 543–565.

Horrit MS, Bates PD, Mattison MJ. 2006. Effects of mesh resolution and topographic representation in 2D finite volume models of shallow water fluvial flow. *Journal of Hydrology* **329**: 306–314. DOI: 10.1016/j.jhydrol.2006.02.016.

Hubbell DW. 1987. Bed load sampling and analysis. In *Sediment transport in gravel-bed rivers*, Thorne CR, Bathurst JC, Hey RD (eds). Wiley: Chichester; 89–118.

Kasvi E, Alho P, Vaaja M, Hyyppä H, Hyyppä J. 2013a. Spatial and temporal distribution of fluvio-morphological processes on a meander point bar during a flood event. *Hydrology Research* **44**: 1022-1039. DOI: 10.2166/nh.2013.091.

Kasvi E, Vaaja M, Alho P, Hyyppä H, Hyyppä J, Kaartinen H, Kukko A. 2013b. Morphological changes on meander point bars associated with flow structure at different discharges. *Earth Surface Processes and Landforms* **38**: 577–590. DOI: 10.1002/esp.3303.

Kleinhans MG. 2010. Sorting out river channel patterns. *Progress in Physical Geography* **34**: 287–326. DOI: 10.1177/0309133310365300.

Kleinhans MG, Brinke W. 2001. Accuracy of cross-channel sampled sediment transport in large sand-gravel-bed rivers. *Journal of Hydraulic Engineering* **127**: 258–269. DOI: 10.1061/(ASCE)0733-9429(2001)127:4(258).

Kleinhans MG, van den Berg JH. 2011. River channel and bar patterns explained and predicted by an empirical and a physics-based method. *Earth Surface Processes and Landforms* **26**: 721–738. DOI: 10.1002/esp.2090.

Lane SN, Bradbrook KF, Richards KS, Biron PA, Roy AG. 1999. The application of computational fluid dynamics to natural river channels: three-dimensional versus two-dimensional approaches. *Geomorphology* **29**: 1–20. DOI: 10.1016/S0169-555X(99)00003-3.

Leendertse JJ, Liu SK. 1975. *A Three-dimensional Model for Estuaries and Coastal Seas*. Volume II: Aspects of computation, R-1764-OWRT. Rand Corporation: Santa Monica, CA.

Leopold LB, Wolman MG. 1960. River meanders. *Bulletin of the Geological Society of America* **71**: 769–794.

Lesser GR, Roelvik JA, van Kester TM, Stelling GS. 2004. Development and validation of a three-dimensional morphological model. *Coastal Engineering* **51**: 883–915. DOI: 10.1016/j.coastaleng.2004.07.014.

Lotsari E, Veijalainen N, Alho P, Käyhkö J. 2010. Impact of climate change on future discharges and flow characteristics of the Tana River, Sub-Arctic northern Fennoscandia. *Geografiska Annaler* **92 A**: 263–284. DOI: 10.1111/j.1468-0459.2010.00394.x.

Lotsari E, Wainwright D, Corner G, Alho P, Käyhkö J. 2014. Surveyed and modelled one-year morphodynamics in the braided lower Tana River. *Hydrological Processes* **28**: 2685–2716. DOI: 10.1002/hyp.9750.

Lotsari E, Vaaja M, Flener C, Kaartinen H, Kukko A, Kasvi E, Hyyppä H, Hyyppä J, Alho P. Online. Annual bank and point bar morphodynamics of a meandering river determined by high-accuracy multitemporal laser scanning and flow data. Water Resources Research. DOI: 10.1002/2013WR014106.

van Maren DS. 2007. Grain size and sediment concentration effects on channel patterns of silt-laden rivers. *Sedimentary Geology* **202**: 297–316. DOI: 10.1016/j.sedgeo.2007.04.001.

McGowen JH, Garner LE. 1970. Physiographic features and stratification types of coarse-grained point bars: modern and ancient examples. *Sedimentology* **14**: 77–111. DOI: 10.1111/j.1365-3091.1970.tb00184.x.

Muste M, Yu K, Spasojevic M. 2004. Practical aspects pf ADCP data use for quatification of mean river flow characteristics; Part I: moving-vessel measurements. *Flow Measurement and Instrumentation* **15**: 1-16.

Nicholas AP. 2000. Modelling bed load yield in braided gravel bed rivers. *Geomorphology* **36**: 89–106. DOI: 10.1016/S0169-555X(00)00050-7.

Nicholas AP. 2003. Investigation of spatially distributed braided river flows using a two dimensional hydraulic model. *Earth Surface Processes and Landforms* **28**: 655-674. DOI: 10.1002/esp.491.

Nicholas AP. 2013. Modelling the continuum of river channel patterns. *Earth Surface Processes and Landforms* **28**: 1187-1196. DOI: 10.1002/esp.3431.

Nicholas AP, Smith GHS. 1999. Numerical simulation of flow hydraulics in a braided channel. *Hydrological Processes* **13**: 913–929. DOI: 10.1002/(SICI)1099-1085(19990430)13:6<913::AID-HYP764>3.0.CO;2-N.

Nicholas AP, Sandbach SD, Ashworth PJ, Amsler ML, Best JL, Hardy RJ, Lane SN, Orefo O, Parsons DR, Reesink AJH, Sambrook Smith GH, Szupiany RN. 2012. Modelling hydrodynamics in the Rio Paraná, Argentina: an evaluation and inter-comparison of reduced-complexity and physics based models applied to a large sand-bed river. *Geomorphology* **169–170**: 192–211. DOI: 10.1016/j.geomorph.2012.05.014.

Nystrom EA, Rehman CR, Oberg KA. 2007. Evaluation of mean velocity and turbulence measurements with ADCPs. *Journal of Hydraulic Engineering* **133**: 1310–1318. DOI: 10.1061/(ASCE)0733-9429(2007)133:12(1310).

Papanicolaou AN, Elhakeem M, Krallis G, Prakash S, Edinger J. 2008. Sediment transport modelling review – current and future developments. *Journal of Hydraulic Engineering* **134**: 1–14. DOI: 10.1061/(ASCE)0733-9429(2008)134:1(1).

Pinto L, Fortunato AB, Freire P. 2006. Sensitivity analysis of non-cohesive sediment transport formulae. *Continental Shelf Research* **26**: 1826–1839. DOI: 10.1016/j.csr.2006.06.001.

van Rijn LC. 1984a. Sediment transport, part I: bed load transport. *Journal of Hydraulic Engineering* **110**: 1431–1456. DOI: 10.1061/(ASCE)0733-9429(1984)110:10(1431).

van Rijn LC. 1984b. Sediment transport, part II: suspended load transport. *Journal of Hydraulic Engineering* **110**: 1613–1640.

van Rijn LC. 1993. *Principles of Sediment Transport in Rivers, Estuaries and Coastal Seas*. Aqua Publications: The Netherlands.

Rodriguez JF, Bombardelli FA, Garcia MH, Frothingham KM, Rhoads BL, Abad JD. 2004. High-resolution numerical simulation of flow through a highly sinuous river reach. *Water Resources Management* **18**: 177–199. DOI: 10.1023/B:WARM.0000043137.52125.a0.

Rüther N, Olsen NRB. 2007. Modelling free-forming meander evolution in a laboratory channel using three-dimensional computational fluid dynamics. *Geomorphology* **89**: 308–319. DOI: 10.1016/j.geomorph.2006.12.009.

Ryan SE, Porth LS. 1999. A field comparison of three pressure-difference bedload samplers. *Geomorphology* **30**: 307–322. DOI: 10.1016/S0169-555X(99)00059-8.

Schuurman F, Marra WA, Kleinhans MG. 2013. Physics-based modeling of large braided sand-bed rivers: Bar pattern formation, dynamics, and sensitivity. *Journal of Geophysical Research: Earth Surface* **118**: 2509–2527. DOI: 10.1002/2013JF002896.

Shimizu Y, Yamaguchi H, Itakura T. 1990. Three-dimensional computation of flow and bed deformation. *Journal of Hydraulic Engineering* **116**: 235–253. DOI: 10.1061/(ASCE)0733-9429(1990)116:9(1090).

Stelling GS, Leendertse JJ. 1992. Approximation of convective processes by cyclic AOI methods. In *Estuarine and Coastal Modeling, Proceedings 2nd Conference on Estuarine and Coastal Modelling*, Spaulding ML, Bedford K, Blumberg A (eds). ASCE: Tampa; 771–782.

Szupiany RN, Amsler ML, Best JL, Parsons DR. 2007. Comparison of fixed- and moving-vessel flow measurements with an aDp in a large river. *Journal of Hydraulic Engineering* **133**: 1299–1309. DOI: 10.1061/(ASCE)0733-9429(2007)133:12(1299).

Termini D, Piraino M 2011. Experimental analysis of cross-sectional flow motion in a large amplitude meandering bend. *Earth Surface Processes and Landforms* **36**: 244–256. DOI: 10.1002/esp.2095.

Verhaar PM, Biron PM, Ferguson RI, Hoey TB. 2008. A modified morphodynamic model for investigating the response of rivers to short-term climate change. *Geomorphology* **101**: 674–682. DOI: 10.1016/j.geomorph.2008.03.010.